DOI:
10.1016/j.chaos.2024.114809

Dynamically selected steady states and criticality in non-reciprocal networks

Carles Martorell,[1] Rubén Calvo,[1] Alessia Annibale,[2] and Miguel A. Muñoz[1]
[1)] *Departamento de Electromagnetismo y Física de la Materia and Instituto Carlos I de Física Teórica y Computacional, Universidad de Granada, E-18071, Granada, Spain*
[2)] *Department of Mathematics, King's College London, SE11 6NJ London, United Kingdom*

We consider a simple neural network model, evolving via non-linear coupled stochastic differential equations, where neural couplings are random Gaussian variables with non-zero mean and arbitrary degree of reciprocity. Using a path-integral approach, we analyze the dynamics, averaged over the network ensemble, in the thermodynamic limit. Our results show that for any degree of reciprocity in the couplings, two types of criticality emerge, corresponding to ferromagnetic and spin-glass order, respectively. The critical lines separating the disordered from the ordered phases is consistent with spectral properties of the coupling matrix, as derived from random matrix theory. As the non-reciprocity (or asymmetry) in the couplings increases, both ordered phases diminish in size, ultimately resulting in the disappearance of the spin-glass phase when the couplings become anti-symmetric. We investigate non-fixed point steady-state solutions for uncorrelated interactions. For such solutions the time-lagged correlation function evolves according to a gradient-descent dynamics on a potential, which depends on the stationary variance. Our analysis shows that in the spin-glass region, the variance dynamically selected by the system leads the correlation function to evolve on the separatrix curve, limiting different realizable steady states, whereas in the ferromagnetic region, a fixed point solution is selected as the only realizable steady state. In the spin-glass region, stationary solutions are unstable against perturbations that break time-translation invariance, indicating chaotic behavior in large single network instances. Numerical analysis of Lyapunov exponents confirms that chaotic behaviour emerges throughout the spin-glass region, for any value of the coupling correlations. While negative correlations increase the strength of chaos, positive ones reduce it, with chaos disappearing for reciprocal (i.e. symmetric) couplings, where marginal stability is attained. On the other hand, in finite size non-reciprocal networks, fixed points and limit cycles can arise in the spin-glass region, especially close to the critical line. Finally, we show that chaos is suppressed when the strength of external noise exceeds a certain threshold. Intriguing analogies between chaotic phases in non-equilibrium systems and spin-glass phases in equilibrium are put forward.

Significance statement:

Diverse equilibrium systems with heterogeneous interactions lie at the edge of stability. Such marginally stable states are dynamically selected as the most abundant ones or as those with the largest basins of attraction. On the other hand, systems with non-reciprocal (or asymmetric) interactions are inherently out of equilibrium, and exhibit a rich variety of steady states, including fixed points, limit cycles and chaotic trajectories. How are steady states dynamically selected away from equilibrium? We address this question in a simple neural network model, with a tunable level of non-reciprocity. Our study reveals different types of ordered phases and it shows how non-equilibrium steady states are selected in each phase. In the spin-glass region, the system exhibits marginally stable behaviour for reciprocal (or symmetric) interactions and it smoothly transitions to chaotic dynamics, as the non-reciprocity (or asymmetry) in the couplings increases. Such region, on the other hand, shrinks and eventually disappears when couplings become anti-symmetric. Our results are relevant to advance the knowledge of disordered systems beyond the paradigm of reciprocal couplings, and to develop an interface between statistical physics of equilibrium spin-glasses and dynamical systems theory.

I. INTRODUCTION

Countless systems, both natural and human-made — such as species in ecosystems, neurons in neural networks, agents in financial markets and atomic magnetic moments in disordered materials— can be visualized as heterogenous networks of interacting elements. In the case of fully connected systems with symmetric or reciprocal interactions, the general phenomenology is that upon increasing the heterogeneity in pairwise interactions, there is a transition from a phase with a single equilibrium to a "spin-glass" phase with multiple equilibria[1–4]. The latter is characterized by ergodicity breaking, slow dynamics, memory, and the breakdown of time-translation invariance (TTI) among other non-trivial features. The spin-glass (SG) phase exhibits a complex energy landscape with many minima, separated by large barriers, hence different copies or "*replicas*" of the system typically relax in distinct regions of the phase space[1]. This leads to the phenomenon of replica-symmetry breaking (RSB), namely the breakdown of symmetry among different replicas, when averaging over the distribution of interactions[1]. It is well-known that there are two main classes of RSB, the one-step RSB (1RSB) and the full RSB (fRSB), and that these are characterized by a different structure of the metastable states: marginal (and unstable under external perturbations) in fRSB and well-shaped and surrounded by large barriers in 1RSB[5–7].

Many systems in different situations (physics, biology, ecology, neuroscience and economics) are intriguingly observed to lie just at the edge of stability or operate near criticality[8–17]. The recent application of RSB frameworks to some of such systems has been highly revealing, suggesting that they may dynamically select marginally stable states, as they could be the most numerous and/or those with the largest basins of attraction, underpinning a fRSB scenario[18–23]. Such a powerful framework, however, is limited to equilibrium systems with reciprocal (or symmetric) interactions, which preserve detailed balance.

For systems with non-reciprocal interactions, a general framework to quantify the rich diversity of emerging steady states, typically including limit cycles and chaotic trajectories, in addition to fixed points, is yet to be established —although recent years have seen some progress in this direction[24–28]— and there is, as yet, no method to predict which steady state is dynamically selected by the system.

It is known that systems with asymmetric interactions can exhibit a transition to chaotic behaviour as the randomness in their interactions is increased[29,30] as well as exotic so-called *non-reciprocal* phase transitions[31], that constitute a topic of current research interest.

In addition, it has been shown that, for asymmetric neural networks close to the transition into a chaotic phase, the mean number of fixed points diverges exponentially with network size, with the rate of divergence, called *topological complexity*, following the trend of the largest Lyapunov exponent[32]. However, how topological complexity affects dynamical complexity remains unclear; indeed, a formal connection between spin-glass-like phases with exponentially many equilibria and chaotic dynamics has not been established yet.

The aim of this manuscript is to advance the development of an interface between the statistical physics of classical disordered systems and dynamical systems theory, by showing that chaotic phases in non-equilibrium systems exhibit certain analogies with spin glass phases in equilibrium (fRSB) systems.

We revisit a classical model for neural networks dynamics —introduced by Sompolinsky, Crisanti and Sommers in[29]— and modify it to allow for interactions to be unbalanced (i.e. with a non-vanishing mean) and *randomly* asymmetric, as well as to incorporate "thermal noise" in the dynamics.

We bypass the (hard) problem of calculating the topological complexity of different attractors in the configuration space and focus on dynamical aspects (e.g. time-dependent moments) of the trajectories at stationarity, as originally proposed by SCS in[29].

By computing two order parameters, namely the mean and variance of neural activity, we reveal the emergence of two types of criticality, one corresponding to ferromagnetic order and the other corresponding to spin-glass order. The transition from the disordered to the ordered phase can be rationalised in terms of spectral properties of the interactions matrix.

Numerical analysis of the largest Lyapunov exponents (LLE) shows that chaotic dynamics arises in the spin-glass region of the phase diagram, for any value of the asymmetry of the couplings.

For uncorrelated couplings, we analyse the non-fixed point steady states and we determine the value of the variance that is *dynamically* selected by the system. We find that whenever the parameters allow for the existence of a multitude of physical (i.e. realizable) steady-state solutions, the system selects the steady state corresponding to the separatrix curve, which delimitates the basins of attractions of different steady states. This is reminiscent of the behaviour of fRSB systems at equilibrium, which select *marginally stable* states, i.e. saddles in the free-energy landscape, that are linked together by flat directions. Our analysis suggests that chaotic motion is the manifestation, at the level of *single network instances*, of such an ensemble averaged dynamics lying on the separatrix curve, delimiting different *realizable* steady states. Such a motion is not time-translation invariant, similarly to ageing dynamics in spin-glass phases. Finally, we show that upon increasing the signal (i.e. the imbalance of interactions), or the thermal noise, the system is brought to a phase where only one bounded solution exists and chaos is suppressed. Such a behaviour can be seen again, as mirroring equilibrium phase transitions from spin-glass phases (with many equilibria) to ferromagnetic or paramagnetic phases (with a single equilibrium), when the signal or the noise, respectively, are raised above a critical value.

The manuscript is organized as follows: In Sec. II, we define the model. Sec. III delves into the linear stability of the quiescent state, revealing the existence of two types of criticality. Sec. IV explores the dynamics of the model via a path integral formalism. In particular, we first consider the dynamics in the absence of noise for uncorrelated interactions (Sec. IV A). Then, we shift our focus to the noisy dynamics for uncorrelated interactions (Sec. IV B). Finally, we analyze the case of correlated interactions (Sec. IV C). We discuss the main results and conclusions in Sec. V. For further technical details and complementary analyses, readers can refer to the Appendices and the Supplementary Material (SM).

II. RATE MODEL

We consider a variant of the classical model introduced by Sompolinsky, Crisanti and Sommers (SCS) in[29]. The model consists of a fully-connected network with N neurons (as shown Fig. 1, left panel), each one described by its time-dependent firing rate, $x_i(t)$, with $i = 1, 2, ..., N$. Their dynamics obey the following set of coupled stochastic differential equations

$$\dot{x}_i = -x_i + f\Big(g \sum_j J_{ij} x_j + \theta_i\Big) + \xi_i, \quad i = 1, \dots, N \quad (1)$$

where the first term on the right hand side describes a spontaneous decay of activity; the second one is the re-

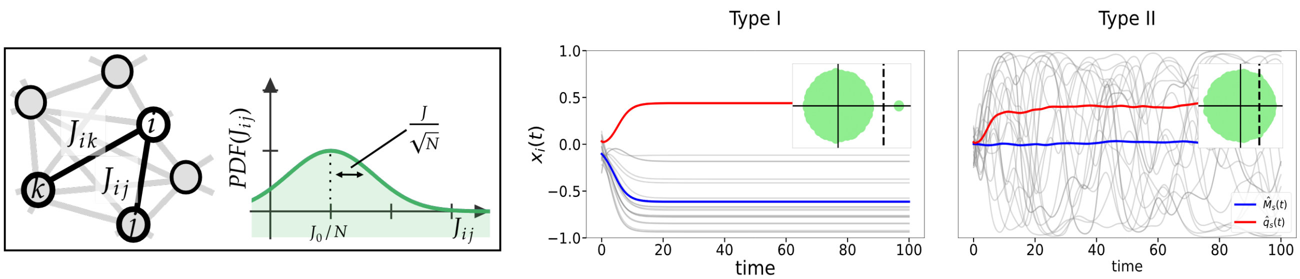

FIG. 1. The left panel illustrates a fully-connected network with N nodes and coupling strengths J_{ij}, drawn randomly and independently from a Gaussian distribution with mean J_0/N and variance J^2/N. The central and right panels sketch typical trajectories, $x_i(t)$, obtained from a numerical simulation of Eq. (1) for a network instance (with $\gamma = 0$). The trajectories of a few nodes (solid grey lines) are plotted together with the mean $\hat{M}(t) = N^{-1}\sum_i x_i(t)$ (blue line) and variance $\hat{q}(t) = N^{-1}\sum_i x_i^2(t)$ (red line). For type-I phase transitions (central panel), the trajectories converge to steady-state values (on the same timescale) while for type-II (right panel) trajectories are highly irregular or chaotic. The insets show the distribution of eigenvalues (in the complex plane) for each case: for type-I transitions, only one eigenvalue, the outlier, has crossed the line $\mathrm{Re}[\lambda] = 1/g$ (shown by the dashed line), while for type-II, a section of the bulk has crossed the line (without a gap), giving rise to a more complex dynamics.

sponse to inputs, mediated by the gain function $f(x)$ which is a monotonically increasing function which saturates for large (in absolute value) arguments, taken here, without loss of generality, to be $f(x) = \tanh(x)$; g is an overall coupling strength and the "synaptic weights", J_{ij}, are (quenched) Gaussian random variables with mean J_0/N and variance J^2/N

$$\overline{J_{ij}} = \frac{J_0}{N}; \qquad \overline{J_{ij}^2} - \frac{J_0^2}{N^2} = \frac{J^2}{N} \tag{2}$$

where overbars stand for network average. We allow for correlations between J_{ij} and its reciprocal, J_{ji},

$$\overline{J_{ij}J_{ji}} - \frac{J_0^2}{N^2} = \gamma\frac{J^2}{N} \tag{3}$$

quantified by the Pearson's correlation coefficient $\gamma \in [-1, 1]$, so that for $\gamma = 1$, interactions are symmetric/reciprocal i.e. $J_{ij} = J_{ji}$, for $\gamma = 0$ they are uncorrelated (or so-called "fully asymmetric"), and for $\gamma = -1$ they are anti-symmetric. The external field θ_i is added to generate response functions and will be set to zero afterwards. Finally, the third term, $\xi_i(t)$, is a zero-mean Gaussian white noise with $\langle \xi_i(t)\xi_j(t')\rangle = 2\sigma^2\delta_{ij}\delta(t-t')$, so that σ is the noise amplitude, and $\langle ...\rangle$ stands for noise average.

Let us remark that this model is very similar to the classical one of SCS but differs in a few aspects: (i) the non-linear function applies to the sum of inputs rather than to each of them; this brings the model closer to rate models in neuroscience[33]; (ii) the connectivity matrix is allowed here to have a non-vanishing mean, so that one can study "excitation" ($J_0 > 0$) and "inhibition" ($J_0 < 0$) dominated regimes (we refer to these as "unbalanced" cases); (iii) interactions have an *arbitrary* degree of symmetry/reciprocity (encoded in γ); (iv) noise $\sigma^2 \neq 0$ is included in the dynamics.

In what follows, we discuss two alternative approaches to tackle analytically different aspects of the model: (i) a linear stability analysis of the fixed points of the noiseless dynamics, allowing us to compute phase boundaries and (ii) a more complete path-integral formalism, allowing for a full (dynamic mean-field) solution (exact in the infinite network-size limit).

III. LINEAR-STABILITY ANALYSIS

To scrutinize the possible steady states of the noiseless dynamics we start by considering a linear stability analysis of the "quiescent" solution, where $x_i(t) = 0$, $\forall i = 1, \dots, N$ and the neural network remains inactive. For this we fix $\theta_i = 0$, $\sigma_i = 0$ in Eq. (1), and expand $f(x)$ to the first order

$$\dot{x}_i = -x_i + g\sum_j J_{ij}x_j, \quad i = 1, \dots, N.$$

Thus, the stability of the quiescent solution is controlled by the largest eigenvalue, λ_M, of the connectivity matrix $\mathbf{J}$, which depends on the model parameters (J_0, J) as well as the degree of correlation, γ. In particular, the quiescent solution is stable if $g\lambda_M < 1$, and becomes unstable for values of g above $g_c = 1/\lambda_M$.

The maximum eigenvalue can be easily computed (in the infinite network-size limit) using well-known results from random matrix theory (RMT) for the case of fully asymmetric ($\gamma = 0$) and symmetric ($\gamma = 1$) networks. In particular, for fully asymmetric networks with $|J_0| < J$ the eigenvalues obey the Girko's circle law, meaning they lay uniformly inside a circle of (spectral) radius J in the complex plane centered at the origin[34–36], i.e. the maximum eigenvalue coincides with J. If, however, $|J_0| > J$, then one of the eigenvalues leaves the circle becoming a real-valued "outlier" with value ${J_0}^{36,37}$. On the other hand, for symmetric networks, with $|J_0| < J$, the eigenvalues are all real and obey the Wigner's semicircle law, so that they are uniformly distributed on a semicircle of radius $2J$[38], i.e. the maximum eigenvalue coincides with $2J$. For symmetric networks with $|J_0| > J$, the distribution of the bulk keeps following Wigner's law, but a single outlier eigenvalue appears at $J_0 + J^2/J_0$[39].

Hence, the limit of stability, g_c, is given by the largest element between the outlier and the largest eigenvalue in the bulk, i.e. one has, for $\gamma = 0$

$$g_c \max(J, J_0) = 1 \rightarrow \frac{1}{g_c J} = \max\Big(1, \frac{J_0}{J}\Big) \tag{4}$$

while, for $\gamma = 1$

$$g_c \max\left(2J, J_0 + \frac{J^2}{J_0}\right) = 1 \rightarrow \frac{1}{g_c J} = \max\Big(2, \frac{J_0}{J} + \frac{J}{J_0}\Big). \tag{5}$$

Furthermore, for general γ's, the distribution of eigenvalues has been derived for balanced matrices in[40], and the position of the outlier has been calculated for unbalanced matrices in[41].

Thus, depending on whether the largest eigenvalue is an outlier or is at the edge of the bulk, two different paths to instability emerge. If the outlier is the largest eigenvalue, as g is increased, a single collective mode (given by the eigenvector associated to the outlier eigenvalue) destabilizes, as illustrated in the central panel of Fig.1. In this case, the system reaches a fixed steady state above the instability threshold. If, on the other hand, the maximum eigenvalue lies at the edge of the bulk, a continuum of modes may become destabilized as g is increased across the edge of instability, as illustrated in Fig.1, right panel. In this case, the dynamics of the system turns out to be non-trivial and complex trajectories emerge. This difference is the core of the distinction between type-I and type-II criticalities[42,43].

It is important to highlight that linear stability analysis does not enable us to characterize the two types of criticality in terms, for example, of order parameters and critical exponents, nor does it help us to locate the transition between type-I and type-II phases, away from the quiescent state. Thus, to tackle analytically this general problem one needs to resort to a more sophisticated dynamical mean-field approach as developed in the following section.

Before concluding this section, it is worth remarking that a linear stability analysis of the symmetrized matrix ($\mathbf{H} = \frac{1}{2}(\mathbf{J} + \mathbf{J}^T) - \mathbf{I}$)[44–47] enables us to discern a regime within the linearly stable phase where the dynamics is "reactive". This implies that perturbations are amplified before returning to the steady state. Reactive dynamics has been extensively discussed in neuroscience, and significant functional advantages have been attributed to it[48,49]. In SM Sec. S.IV we show that the model under study exhibits such regimes of reactivity.

IV. PATH-INTEGRAL FORMALISM

To analyze the full phase diagram one can resort to a "dynamic mean-field" approach (DMF) as originally introduced by SCS[29] and later developed in a number of works (e.g,[50–53]). Alternatively, one can employ a more systematic path-integral formalism (or generating functional analysis) as originally introduced by Martin, Siggia and Rose[54] and successfully applied to neural networks in[55–57], which allows to formally derive the DMF equations and quantify their limits of validity[50,57]. The calculation is quite standard but, for the sake of completeness, here we reproduce the main steps.

The starting point of the method is the definition of the moment-generating functional of the random (vector) function $\mathbf{x}(t)$

$$Z[\boldsymbol{\psi}] = \Big\langle e^{i\ \sum_i \int dt\, x_i(t)\psi_i(t)} \Big\rangle \tag{6}$$

where the average $\langle \dots \rangle$ is taken over the probability distribution $P[\mathbf{x}(t)]$ of trajectories $\mathbf{x}(t)$, generated by Eq.(1), for a fixed (quenched) connectivity matrix $\mathbf{J}$. From such a generating functional one can easily compute the chief quantities describing the system's collective dynamics, such as the mean activity of a neuron i

$$M_i(t) = \langle x_i(t) \rangle = \left.\frac{\delta Z[\boldsymbol{\psi}]}{i\delta\psi_i(t)}\right|_{\boldsymbol{\psi}=\mathbf{0}}, \tag{7}$$

the two-time pairwise correlations

$$C_{ij}(t,t') = \langle x_i(t) x_j(t') \rangle = \left.\frac{\delta Z[\boldsymbol{\psi}]}{i\delta\psi_i(t) i\delta\psi_j(t')}\right|_{\boldsymbol{\psi}=\mathbf{0}}, \tag{8}$$

and the response functions

$$R_{ij}(t,t') = \frac{\delta\langle x_i(t)\rangle}{\delta\theta_j(t')} = \left.\frac{\delta^2 Z[\boldsymbol{\psi}]}{i\delta\theta_j(t')\delta\psi_i(t)}\right|_{\boldsymbol{\psi}=\mathbf{0}}. \tag{9}$$

In order to compute disorder-averaged quantities, one needs to average the generating functional $Z[\boldsymbol{\psi}]$ over the distribution $P(\mathbf{J})$. This procedure leads —once the infinite network-size ($N \rightarrow \infty$) limit has been taken— to a self-consistent stochastic equation for the dynamics of a *representative* neuron, called dynamical-mean-field equation[29,50,58], see Supplemental Material (SM) Sec. S.I for further details:

$$\dot{x}(t) = -x(t) + \tanh\left[J_0 g M(t) + \gamma J^2 g^2 \int dt'\, R(t,t') x(t') + \theta(t) + \phi(t)\right] + \xi(t). \tag{10}$$

In this equation, $\xi(t)$ is a zero-mean Gaussian white noise with $\langle\xi(t)\xi(t')\rangle = 2\sigma^2\delta(t-t')$, $\phi(t)$ is a random Gaussian field with zero mean and auto-correlation

$$\langle\phi(t)\phi(t')\rangle = J^2g^2C(t,t') \tag{11}$$

and the order parameters $M(t)$, $C(t,t')$ and $R(t,t')$ need to be calculated self-consistently, as averages over realizations of the effective single-neuron process:

$$M(t) = \langle x(t)\rangle, \tag{12}$$
$$C(t,t') = \langle x(t)x(t')\rangle \tag{13}$$
$$R(t,t') = \frac{\delta\langle x(t)\rangle}{\delta\theta(t')} = \langle\frac{\delta x(t)}{\delta\phi(t')}\rangle, \tag{14}$$

where in the second equality of the last equation we have used that θ and ϕ have the same role in Eq.(10). The random function $\phi(t)$ can be interpreted as an "interference" term that quantifies the impact, on the dynamics of the representative neuron, of all the other neurons that interact with it, while the second term in the square brackets of Eq.(10) accounts for the so-called "retarded" self-interactions of the representative neuron with its own past, i.e. past values $x(t')$ influence $x(t)$ at later times $t > t'$. This is due to the fact that the representative neuron sends signal to its neighbours through links which are *correlated* with those used by the neighbours to send signal back to it. We note that (as usual) this term only arises when such correlations in the links are present (i.e. $\gamma \neq 0$) and it makes the effective dynamics non-Markovian. From here on, the external field is fixed to zero, $\theta(t) = 0$.

In the following sections, we investigate separately the cases of (i) uncorrelated interactions ($\gamma = 0$) with noiseless dynamics ($\sigma = 0$); (ii) uncorrelated interactions ($\gamma = 0$) with noisy dynamics ($\sigma \neq 0$) and (iii) correlated interactions ($\gamma \neq 0$), focusing for simplicity on the noiseless case.

A. Uncorrelated interactions ($\gamma = 0$) and noiseless dynamics ($\sigma = 0$)

For uncorrelated interactions (i.e. $\gamma = 0$), the equation of motion for the noiseless dynamics ($\sigma = 0$) takes a particularly simple form

$$\dot{x}(t) = -x(t) + \tanh[J_0gM(t) + \phi(t)], \tag{15}$$

that can be explicitly analyzed.

1. Fixed-point solutions

Let us start by assuming that the system reaches a single stable fixed point $x(t) = x$. In such a case, $\langle x\rangle = M$, $\langle x^2\rangle = C(0) = q$, and each realization of $\phi(t)$ becomes a static zero-mean Gaussian random variable with variance J^2g^2q[59,60]. Therefore, imposing the stationarity condition, $\dot{x} = 0$, in Eq.(15) and averaging over ϕ one readily obtains:

$$\begin{aligned} M &= \langle \tanh(J_0gM + \phi)\rangle \\ &= \int \mathcal{D}\psi \tanh(J_0gM + gJ\sqrt{q}\psi) \end{aligned} \tag{16}$$

where the short-hand notation $\mathcal{D}\psi = e^{-\psi^2/2}d\psi/\sqrt{2\pi}$ has been introduced. Similarly, the variance q at the fixed-point solution is

$$\begin{aligned} q &= \langle \tanh^2(J_0gM + \phi)\rangle \\ &= \int \mathcal{D}\psi \tanh^2(J_0gM + gJ\sqrt{q}\psi). \end{aligned} \tag{17}$$

An alternative, simpler derivation of Eqs.(16)-(17) —not generalizable to the $\gamma \neq 0$ case— is presented in SM (Sec. S.II).

Before proceeding, we note that Eq.(16) and Eq.(17) are identical to the equations for the magnetization and the Edward-Anderson order parameter, respectively, in the well-known Sherrington-Kirkpatrick (SK) model for spin-glasses[61], within a replica symmetric ansatz, with $1/g$ playing the role of the temperature (see e.g. Eqs.(2.28)-(2.30) in[3]). Such an equivalence, at the level of order parameters, between the SK model and the neural-network rate model under study, is surprising as the two models are defined in rather different ways. In particular, the SK model is defined for Ising (i.e. ±1) variables with symmetric interactions while here Eq.(16) and Eq.(17) have been derived for continuous state variables and non-symmetric interaction matrices.

From the analogy with spin glasses, it is well-known that Eq.(16) and Eq.(17) have a trivial disordered solution (referred to as "paramagnetic" in the context of magnetic systems) with $(M, q) = (0, 0)$, which is stable at sufficiently high temperatures (corresponding here to small values of the coupling constant g). From the disordered phase, two different types of order may emerge, depending on the relative values of the mean J_0 and variance J of the coupling distribution.

In particular, for $J_0 > J$, there is a bifurcation at $gJ_0 = 1$ from the disordered phase to an ordered (or "ferromagnetic") phase in which the up-down symmetry is broken, i.e., there is a non-vanishing magnetization, $(M \neq 0, q \neq 0)$. On the other hand, for $J_0 < J$, a bifurcation occurs at $gJ = 1$ from such a disordered phase to a "spin-glass" phase $(M = 0, q \neq 0)$[61]. Therefore, the disordered phase loses its stability at the critical value g_c, given by Eq.(4), in agreement with results from linear-stability analysis. In particular, type-I criticality discussed in Sec. III can be identified with the transition from the paramagnetic to the ferromagnetic phase, while type-II criticality corresponds to the transition from the paramagnetic to the spin-glass phase. Such criticalities can therefore be fully characterised by the order parameters M and q, which correspond to mean neural activity and mean-squared activity, respectively. In addition, the

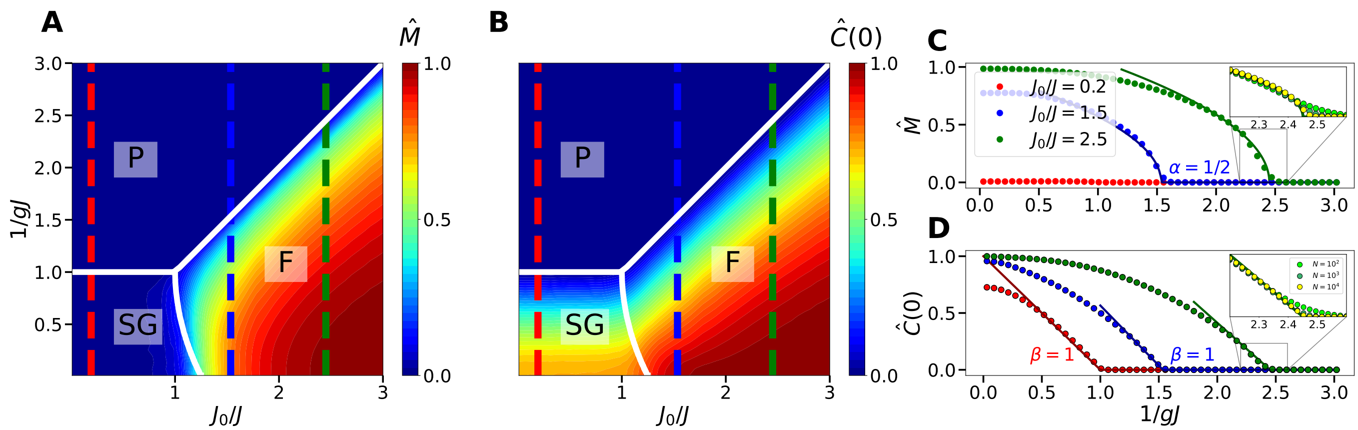

FIG. 2. Phase diagram of the model for **uncorrelated** ($\gamma = 0$) and **noiseless** dynamics ($\sigma^2 = 0$). **Panels (A, B)**: Heat map of the time-averaged mean activity $\hat{M}$ (panel (A)) and mean-squared activity (or equal-time correlator) $\hat{C}(0)$ (panel (B)), obtained from simulations as a function of the control parameters J_0/J (as color coded) and $1/gJ$. The white lines represent the theoretically predicted critical curves (from stability analyses of fixed-point solutions) separating the paramagnetic (P), ferromagnetic (F) and spin-glass (SG) phases. **Panels (C, D)**: Symbols show $\hat{M}$, from panel (A), and $\hat{C}(0)$, from panel (B), obtained from simulations, versus $1/gJ$, at three different values of J_0/J, corresponding to the three dashed vertical lines on (A) and (B). Solid lines show the theoretically predicted asymptotic behaviour around the critical point such that $M \sim (g - g_c)^\alpha$ (defined only for the ferromagnetic transition) and $q \sim (g - g_c)^\beta$. (Note that M and q denote, respectively, the values of the mean and the mean-squared activity obtained from the theory —by averaging over initial conditions and network ensemble—, assuming a fixed-point solution, whereas $\hat{M}$ and $\hat{C}(0)$ denote their numerical counterparts obtained from numerical simulations by averaging over different realizations.) The inset illustrates the effect of increasing the system size ($N = 100, 1000, 10000$).

critical line separating the ferromagnetic from the spin-glass phase can be obtained by analyzing the limit of linear stability of the $M = 0$ solution, which —as derived in the SM (Sec. S.III)— leads to

$$\frac{1}{gJ} = \frac{J_0}{J}(1 - q^*) \tag{18}$$

where q^* is the solution of

$$q^* = \int \mathcal{D}\psi \tanh^2\left(gJ\sqrt{q^*}\psi\right). \tag{19}$$

The resulting phase diagram, in the parameter space $(J_0/J, 1/gJ)$, is shown in Fig.2, where the solid white lines in panels (A) and (B) represent the critical lines separating the paramagnetic (P), ferromagnetic (F) and spin-glass (SG) phases.

Expanding the self-consistency Eqs.(16)-(17) to the first sub-leading order, it is possible to obtain the critical exponents α and β such that $M \sim (g - g_c)^\alpha$ and $q \sim (g - g_c)^\beta$ (see SM, Sec. S.III). For the ferromagnetic transition $J_0 > J$, one has $\alpha = 1/2$ and $\beta = 1$ (as in the Ising model) whereas for the SG transition, i.e. for $J_0 < J$, the exponent α is trivially 0 and $\beta = 1$.

In addition to fixed-point solutions, a rich set of possible non-fixed-point solutions is expected to appear with non-symmetric interactions, including limit cycles and chaotic trajectories[29,51,57]. Among these, stationary solutions are characterised by a time-independent average $M(t) = M$ and a time-translation invariant two-time correlator $C(t, t') = C(t - t')$, which implies a time-independent equal-time correlator $C(t, t) = C(0)$ (note that for fixed-point solutions $C(0) = q$, however for non-fixed-point solutions $C(0) \neq q$). Whenever the steady state is not a fixed point, node activities $x_i(t)$ fluctuate in time, even at stationarity. One can therefore ask whether the phase diagram derived for fixed-points gives reliable information on the phase transition behaviour of the system, whose dynamics is not necessarily at a fixed point.

To address this question, we ran S independent computer simulations of the microscopic dynamics and, assuming that the system eventually reaches a steady-state, we computed the stationary magnetization and equal-time (or zero-lag) correlator for each simulated trajectory $\mathbf{x}_s(t)$, with $s = 1, \ldots, S$, as the sample average of the mean activity[62]

$$\hat{M}_s = \frac{1}{t_m} \sum_{t=t_0}^{t_0+t_m} \frac{1}{N} \sum_{i=1}^{N} x_{i,s}(t) \tag{20}$$

and mean-squared activity

$$\hat{C}_s(0) = \frac{1}{t_m} \sum_{t=t_0}^{t_0+t_m} \frac{1}{N} \sum_{i=1}^{N} x_{i,s}^2(t) \tag{21}$$

respectively, where $t_m \gg 1$ and t_0 is a sufficiently long time to allow the dynamics to relax to stationarity. Fig.2 shows a heat map of their averages $\hat{M} = S^{-1}\sum_{s=1}^{S} |\hat{M}_s|$ (panel (A)) and $\hat{C}(0) = S^{-1}\sum_{s=1}^{S} \hat{C}_s(0)$ (panel (B)), where the absolute value $|...|$ is used to avoid the cancellation between positive and negative states of the system.

Simulations are performed with $S = 1000$ realizations, for a system with size $N = 1000$, for different values of the parameters $(J_0/J, 1/gJ)$. Notably, the phase diagram derived for fixed-point solutions captures very well the phase transition behaviour of $\hat{C}(0)$ and $\hat{M}$, which vanish in the disordered (paramagnetic) phase and become non-zero in the ordered (spin-glass and ferromagnetic) phases. In addition, their asymptotic behaviour close to criticality matches the scaling theoretically predicted for fixed-point solutions (see Fig.2 panels (C) and (D) and SM, Sec. S.III for details). This suggests that close to the instability line of the paramagnetic phase, trajectories are at a fixed point. This is consistent with bifurcation analysis, showing that the first non-trivial steady-state solutions to appear below criticality are fixed-point solutions (see SM, Sec. S.V B for details). In the next subsection, we study in detail non-fixed-point solutions at stationarity.

2. Non-fixed point steady states

Let us now focus on stationary solutions other than fixed points. These are characterised by a constant first moment $M(t) = M$ and time-translation invariant correlator $C(t, s) = C(t - s)$, where M is given by

$$M = \int \mathcal{D}\psi \tanh(J_0 g M + gJ\sqrt{C(0)}\psi) \tag{22}$$

with $C(0)$ denoting the equal-time correlator, while the two-time correlator $C(\tau)$ satisfies

$$(1 - \partial_\tau^2)\, C(\tau) = \Xi(C(\tau), C(0), M) \tag{23}$$

with

$$\Xi(C, C(0), M) = \int \mathcal{D}_{\phi\phi'} \tanh[J_0 g M + \phi] \tanh[J_0 g M + \phi'] \tag{24}$$

where

$$\mathcal{D}_{\phi\phi'} = \frac{d\phi d\phi'}{2\pi g^2 J^2 \sqrt{\det \mathbf{C}(\tau)}} \exp\left(-\frac{\boldsymbol{\phi}^T \mathbf{C}^{-1}(\tau)\boldsymbol{\phi}}{2J^2 g^2}\right), \tag{25}$$

see SM, Sec. S.V A for details.

For $\mathbf{C}$ to be positive definite, we must have $C^2(0) \geq C^2(\tau)$, i.e. $C(0) \geq |C(\tau)|$, as expected for a stationary process, where the correlation function (at any time-lag τ larger than 0) is bounded to be smaller than the variance. An expression for the variance $C(0)$ is provided in the SM (Sec. S.V A), however, let us remark that it requires the knowledge of the time-dependent (or "non-persistent") order parameter $C(\tau)$, consistently with earlier findings in asymmetrically diluted recurrent neural networks[56]. Hence, the equations for the time-invariant (or "persistent") order parameters M and $C(0)$ are not a closed set (not even at stationarity), when the system is not at a fixed point. Only when the system is at a fixed point, i.e. $x(t) = x$, then $C(0) = q$ and the equations for M and q form a closed set.

Following[57], we note that Eq.(23) can be cast in a gradient-descent equation

$$\partial_\tau^2 C(\tau) = -\frac{\partial V(C|C(0), M)}{\partial C} \tag{26}$$

on the potential

$$V(C|C(0), M) = -\frac{C^2}{2} + \int_0^C dC'\, \Xi(C', C(0), M) \tag{27}$$

which depends on the persistent order parameters M and $C(0)$.

Note that for $J_0 = 0$, the previous potential reduces to the one governing the correlation function in the model of SCS[29]. Although such an equivalence might seem surprising —given that in the model of SCS, unlike ours, the sum over j in Eq.(1) appears outside the hyperbolic tangent— it can be rationalised by a simple argument as explained in App.A.

As already noticed in[57], solutions of Eq.(26) conserve the total energy

$$E = \frac{1}{2}\dot{C}^2 + V(C|C(0), M). \tag{28}$$

Moreover, at stationarity, $C(\tau) = C(-\tau)$, so that $\dot{C}(0) = 0$ and, hence, the initial kinetic energy vanishes. Thus, from energy conservation one has

$$\frac{1}{2}\dot{C}^2(\tau) + V(C|C(0), M) = V(C(0)|C(0), M). \tag{29}$$

Physical solutions must be bounded, i.e. $|C| \leq C(0)$, this requires $V'(C(0)|C(0), M) > 0$ and $V'(-C(0)|C(0), M) < 0$ at the two boundaries $C = \pm C(0)$, respectively (since $\dot{C}(0) = 0$). It can be easily shown that, for any M, $V'(C(0)|C(0), M) < 0$ if $C(0) > q$, hence such initial conditions are unphysical: the system will have to select a stationary value of the equal-time correlator that is smaller or equal than the persistent parameter q.

Let us now study separately the cases (a) $M \neq 0$ and (b) $M = 0$:

a. ***For*** $\mathbf{M \neq 0}$**.** One can show (see SM S.V C) that the potential is a monotonic non-decreasing function for any initial condition $C(0) \leq q$ and that there is only one stationary point, at the boundary of the physical region $C = C(0) = q$ (see Fig.3, panels (A)). Therefore, the only possible bounded steady-state solutions for $M \neq 0$ are fixed-point solutions with $C = q$.

To verify this, we ran S simulations of the microscopic dynamics to obtain trajectories $\mathbf{x}_s(t)$, with $s = 1 \ldots S$ and computed, for each realization s, the equal-time correlator at stationarity $\hat{C}_s(0)$, as defined in Eq.(21). The resulting distribution

$$P(C_0) = \frac{1}{S}\sum_{s=1}^{S} \delta(C_0 - \hat{C}_s(0)) \tag{30}$$

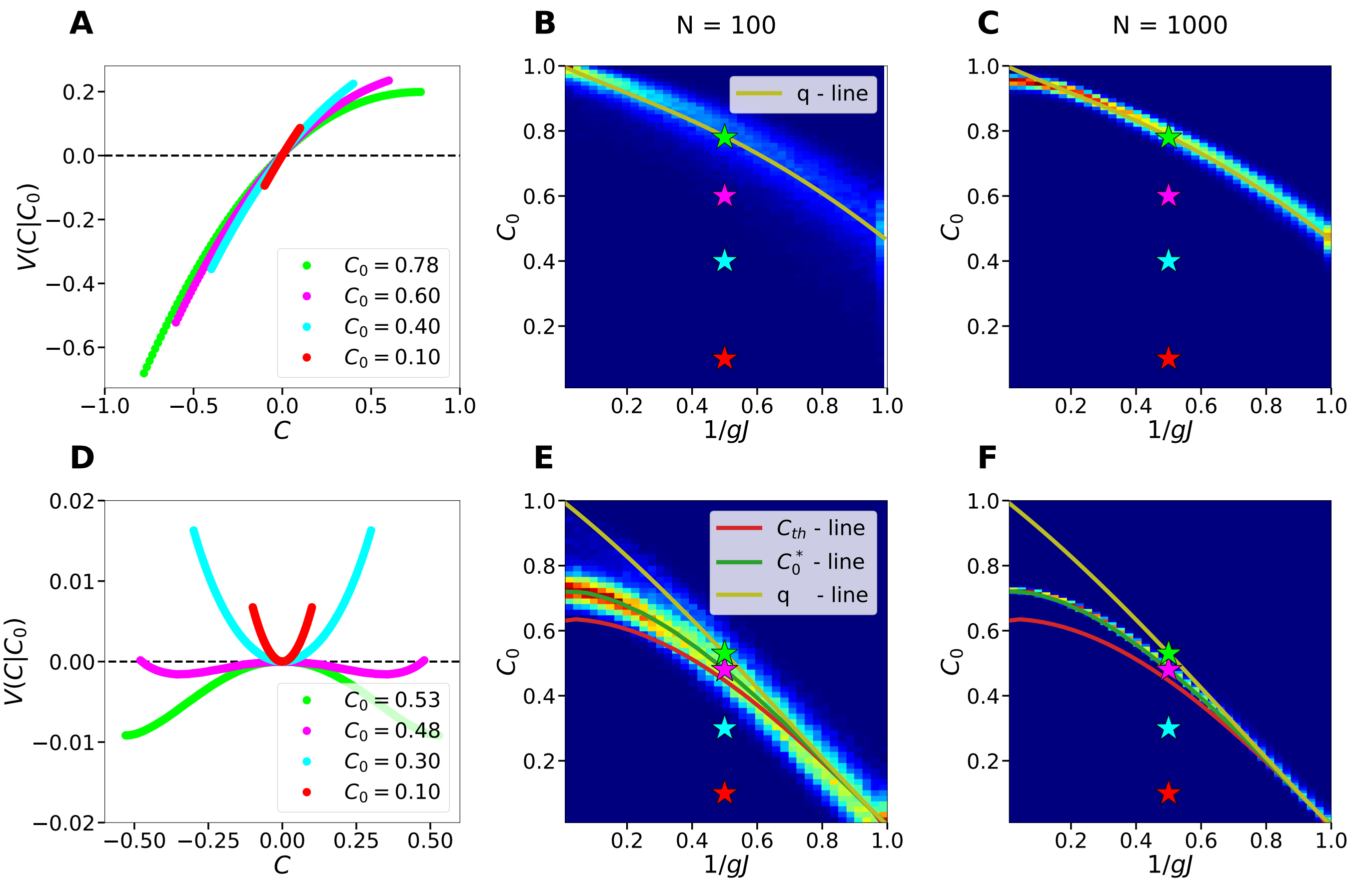

FIG. 3. Analysis of the motion in the effective potential $V(C|C(0), M)$ for the **uncorrelated** ($\gamma = 0$) and **noiseless** ($\sigma^2 = 0$) case. **Panels (A, D)**: potential $V(C|C(0), M)$ as a function of C for $M \neq 0$ (ferromagnetic phase, with $J_0/J = 1.5$) and $M = 0$ (spin-glass phase, with $J_0/J = 0.5$), respectively. Each curve is obtained for a different value of $C(0)$ (as shown in the legend with a color code) and is plotted in the range $C \in [-C(0), C(0)]$. Note that only in the SG phase the potential may exhibit a shape with either one or two wells. The heat maps in panels **(B, C, E, F)** describe the probability distribution function (PDF) $P(C_0)$ (as defined in Eq.(30)) of finding a given value of $C(0)$ for the ferromagnetic case **(B, C)** and the SG phase **(E, F)**, for different values of $1/gJ$ (obtained from $S = 1000$ simulations of the microscopic dynamics, averaged over a time window $t_m = 2000$, for system size $N = 100$ (B, E) and $N = 1000$ (C, F)). Each simulation corresponds to a different realization of the random initial condition and quenched disorder. Stars show the values of $1/gJ$ and $C(0)$ used to plot panels (A, D). In panels (B, C), the solid line ("q-line") describes the solution q obtained from the fixed-point solution, revealing that for large N, the PDF becomes peaked around this value, so that $C(0) = q$. On the other hand, in panels (E, F), the PDF becomes more and more peaked (as the system size is enlarged from $N = 100$ to $N = 1000$) around a value $C_0^* \neq q$, corresponding to the separatrix point (lying in the green curve) at which the potential verifies $V(C(0)|C(0), 0) = 0$ ($C(0) = 0.48$ in (D)). Note that such a green line is in between the q-line (yellow) and the threshold curve $C_{\rm th}$ (red) as described in the main text, so that in particular $C(0) \neq q$ in the SG phase.

is plotted in Fig.3(B, C) as a heat map, for different values of $1/gJ$, two different network sizes N, and a fixed value of J_0/J (corresponding to the ferromagnetic region, i.e. $M \neq 0$). Results show that, as the network size N is increased, the probability density concentrates on the curve corresponding to $C(0) = q$ (solid line), confirming that, indeed, the value of $C(0)$ selected dynamically by the system coincides with q.

b. ***For*** $\mathbf{M = 0}$**.** One can show that —as illustrated in Fig.3 panel (D)— V has the shape of a double-well potential for any initial condition $C(0)$ smaller than q but larger than a certain threshold value $C_{\rm th}$ solution of

$$\int \mathcal{D}\psi \tanh^2(gJ\sqrt{C_{\rm th}}\,\psi) = 1 - \frac{1}{gJ}, \tag{31}$$

whereas below such a threshold ($C(0) < C_{\rm th}$) it becomes a single-well potential (see SM S.V C for further details).

Therefore, any initial condition $0 \leq C(0) \leq q$ leads to bounded solutions, but —depending on the value of $C(0)$ that is dynamically selected by the system— different steady-state solutions may arise as summarized in the following:

- For $0 < C(0) < C_{\rm th}$ the potential has a single-well shape, so that the motion is periodic between $C(0)$ and $-C(0)$.

- For $C_{\rm th} < C(0) < q$, the potential has a double-well shape with a local maximum at $C = 0$, and three possible types of dynamics can emerge:
  - (i) periodic motion in one of the single wells corresponding to motion below the separatrix curve ($C(0) > C_0^*$ such that $V(C(0)|C(0), 0) < 0$);
  - (ii) asymptotic motion towards $C = 0$, corresponding to motion on the separatrix curve ($C(0) = C_0^*$ such that $V(C_0^*|C_0^*, 0) = 0$);
  - (iii) periodic motion between $C(0)$ and $-C(0)$, i.e. covering the two wells, corresponding to motion above the separatrix curve ($C(0) < C_0^*$ such that $V(C(0)|C(0), 0) > 0$).
- For $C(0) = q$, the system remains at the fixed point $C(\tau) = q$ for all values of τ, i.e. the solution is a fixed point.

In Fig.3 (E, F), we show $C_{\rm th}$, C_0^* and q as a function of $1/gJ$ and $C(0)$ (red, green and yellow solid lines, respectively), at a fixed value of J_0/J (corresponding to the spin-glass region, $M = 0$) and for two different system sizes (panel (E), $N = 100$; panel (F), $N = 1000$).

The question that remains to be answered is: what is the value of the equal-time correlation, $C(0)$, that is selected by the system at stationarity? To ascertain this, we plot, in the same figure, the probability distribution function Eq.(30), computed from $S = 1000$ simulations, versus $1/gJ$, as a heat map, for two different system sizes. These results clearly reveal that, as the system size N increases, the probability density concentrates on the curve $C(0) = C_0^*$. This means that in the thermodynamic limit the time-average $C_s(0)$ of any single instance s of the system (obtained for a given initial condition and a particular realization of the quenched disorder) settles precisely on the separatrix curve, i.e. at the boundary that delimits the basins of attraction of the two potential minima $\pm\bar{C}(C_0^*)$. Therefore, the solution sits on an unstable stationary state, where any slight perturbation causes it to move away from the separatrix in either of the two adjacent states.

In particular, in any single network instance the *instantaneous* mean-squared activity after a transitory time t_0

$$\hat{q}_s(t_0 + \tau) = \frac{1}{N}\sum_i x_{i,s}^2(t_0 + \tau) \tag{32}$$

fluctuates in time (τ) about the stationary value $\hat{C}_s(0)$ (unless the system is at a fixed-point steady state). Therefore, in the case in which $\hat{C}_s(0)$ is sufficiently close to C_0^*, such fluctuations can effectively move the system above and below the separatrix as illustrated in Fig.4.

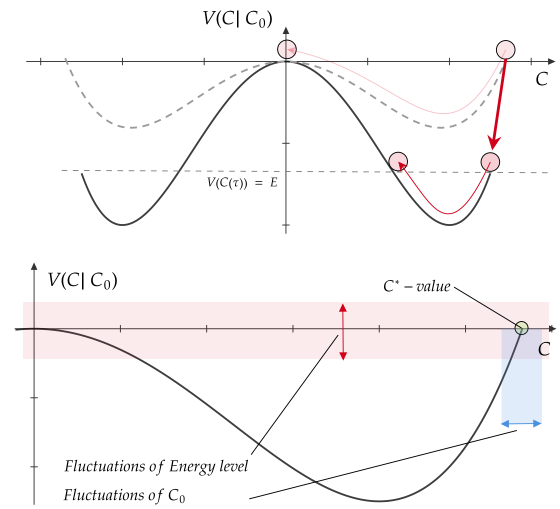

FIG. 4. Illustration of how fluctuations in the initial condition translate into changes in the shape of the potential (upper). Small fluctuations have a large impact when the initial condition varies around the separatrix value C_0^* (lower).

This leads to a motion that is highly irregular and sensitive to perturbations and small changes in initial conditions, as shown in Fig.5(A). As a result, the motion turns out to be chaotic. More specifically: the time-lagged correlator, computed as a sliding time window average over a single dynamical trajectory[63],

$$\hat{C}_s(\tau) = \frac{1}{t_m}\sum_{t=t_0}^{t_m}\frac{1}{N}\sum_i x_{i,s}(t)x_{i,s}(t+\tau) \tag{33}$$

does not exhibit stationary behaviour, but an irregular motion which is not time-translation invariant (TTI), i.e. it retains a dependence on t_0, see Fig.5(A), bottom. Indeed, our analysis in App. B shows that, in the thermodynamic limit, stationary solutions are unstable against perturbations that break TTI, suggesting that such non-TTI steady states are selected in *large* networks.

On the other hand, when $C_s(0)$ is far from C_0^*, small fluctuations cannot shift the system across the separatrix and the resulting motion is periodic, as illustrated in Fig.5(B, C). As a consequence, in *finite* networks of size N, the system exhibits periodic dynamics in wide regions of the phase diagram, where $C_s(0)$ is far from C_0^* (see Fig.3(E)). In addition, Fig.3(E) shows that, at finite N, there is a finite probability that the system exhibits fixed-point dynamics, at sufficiently high values of $1/gJ$.

To illustrate all this, in Fig.6 we show a heat map of the probability of finding fixed-point solutions, versus $J_0/J, 1/gJ$, in a system of (relatively small) size $N = 100$, as well as typical trajectories exhibited by the system at representative points of the phase diagram. Chaotic trajectories are observed only at sufficiently low values of $1/gJ$, where the probability distribution function of $C(0)$

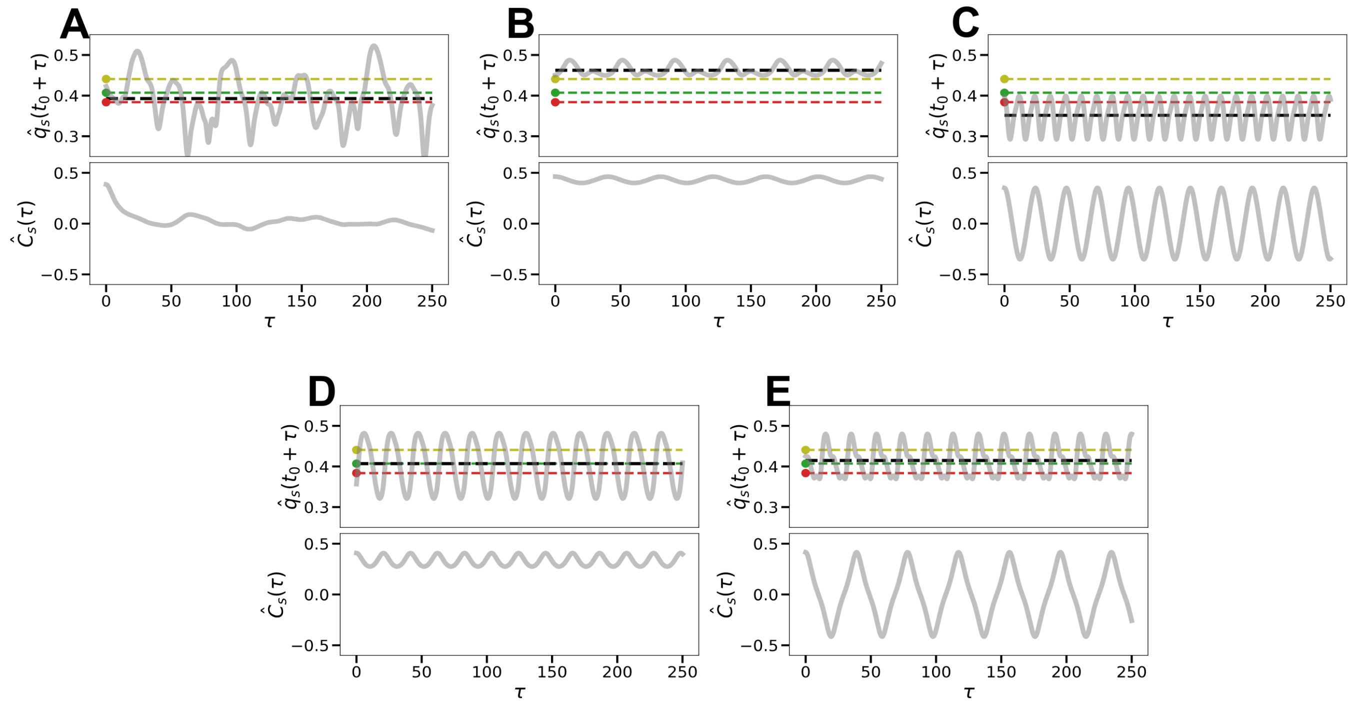

FIG. 5. Single instances of the dynamics for **uncorrelated** ($\gamma = 0$) and **noiseless** dynamics ($\sigma^2 = 0$). The (upper panels) show the time-dependent mean-squared activity $q(t_0+\tau) = N^{-1}\sum_i x_i^2(t_0+\tau)$ (gray line in the upper panels) plotted together with its time average $\hat{C}_s(0)$ and (lower panels) $\hat{C}_s(\tau)$. Curves are obtained from simulations with system size $N = 100$ and $1/gJ = 0.58$ (i.e., within the SG phase). Observe that the trajectories reveal either chaotic behavior (A) or periodic motion (B, C, D, E). The yellow and the red dashed lines show q and $C_{\rm th}$, respectively while the green dashed line –in between the previous two— marks the separatrix C_0^*. In (A) the mean-squared activity fluctuates randomly above and below the separatrix line; in (B, C) the mean-squared activity remains at only one side of the separatrix; in (D, E) the mean-squared activity fluctuates about the separatrix in sync with $\hat{C}_s(\tau)$.

becomes peaked around C_0^*, as shown in Fig.3. Furthermore, we note that, while chaotic trajectories seem to arise, in finite networks, from fluctuations around the separatrix, this does not seem a sufficient condition to have chaotic motion. For example, when fluctuations of the mean-squared activity around the separatrix value are periodic and in sync with the natural oscillations of the two-time correlator, as shown in Fig.5(D, E), the system is observed to settle on a periodic trajectory.

In this regard, the dynamics of the two-time correlator resembles that of a forced oscillator, where the external "force" is given by the fluctuations of the initial condition. In particular, if the driving force is periodic and it has the same frequency as the natural frequency of the oscillator, the system oscillates at the frequency of the applied force as shown in Fig.5(B, D). If the frequency of the applied force is different from the natural frequency of the oscillator, the system may exhibit sub-harmonic oscillations i.e. a periodic motion with a frequency that is a fractional multiple of the input frequency, as shown in Fig.5(C, E).

As discussed earlier, for large N, $C(0)$ is peaked around C_0^*. Therefore, the scenario depicted in Fig. 5(B, C) cannot arise because dynamical fluctuations of the mean-squared activity about its time-averaged value move the system above and below the separatrix curve. However, periodic trajectories as described in Fig.5 (D, E), can in principle still arise. In order to determine whether periodic motion survives for large N, it is therefore important to establish whether such trajectories remain stable in the thermodynamic limit. Our analysis in App. B suggests that they lose stability for large N, as stationary trajectories in the spin-glass region are unstable, in the thermodynamic limit, against perturbations that break TTI.

Numerical evaluation of the largest Lyapunov exponent (LLE) Λ, in simulated trajectories of the system (see App.D 3) shows that, upon increasing N, only chaotic orbits prevail inside the spin-glass region. Fig.7 (A) shows that at small system sizes, Λ is positive for small values of $1/gJ$ within the spin-glass region, and it decreases to zero as $1/gJ$ increases. However, as the system size increases, the value of Λ at $1/gJ = 1$ increases and eventually vanishes (see inset of Fig.7, panel B), suggesting that, in this limit, Λ remains positive for any $1/gJ < 1$. On the other hand, in the ferromagnetic region Λ remains

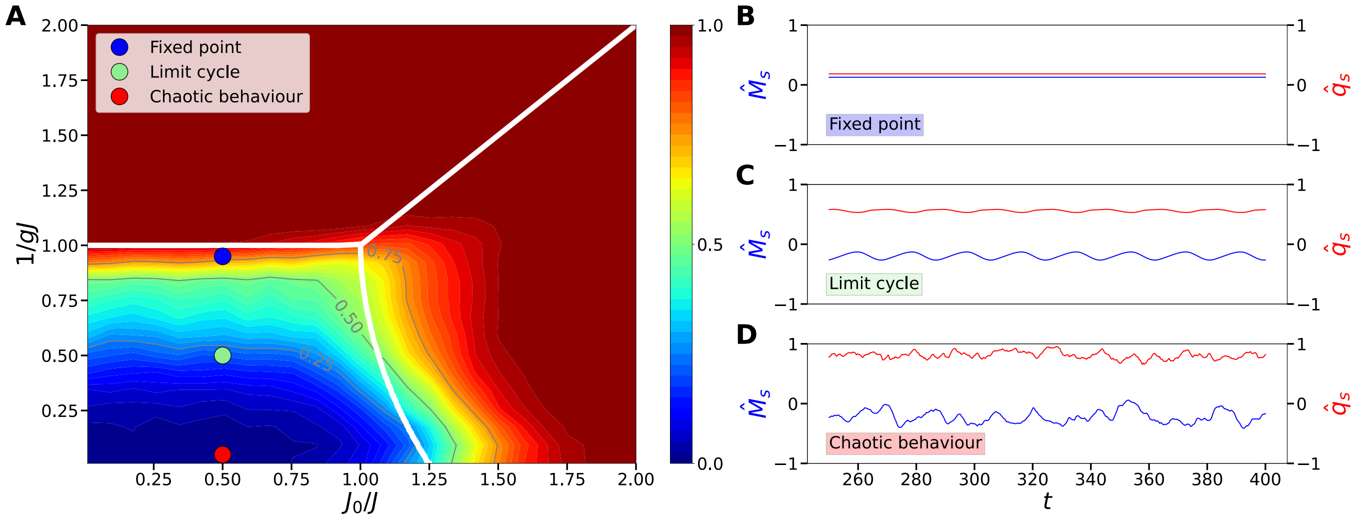

FIG. 6. Probability of finding a fixed-point solution in the **uncorrelated** ($\gamma = 0$) and **noiseless** ($\sigma^2 = 0$) case in simulations with networks of size $N = 100$. **Panel (A)**: Heat map of the PDF of finding a fixed-point solution for $S = 1000$ different realizations of the microscopic dynamics. Such a probability drops as $1/gJ$ is lowered, in agreement with Fig.3, showing that the probability that $C(0) = q$ vanishes at low values of $1/gJ$. In such a region a non-fixed-point solution characterized by chaotic behaviour emerges. **Panels (B, C, D)**: Typical trajectories observed in simulations at different values of the parameters $J_0/J, 1/gJ$ as indicated by circles on (A). Additional studies reveal that, in the thermodynamic limit, chaotic solutions are the only stable solutions throughout the whole spin-glass phase.

negative for any value of $1/gJ$, see Fig.7 (C). The inset in panel (B) indicates that the approach to zero of Λ at $1/gJ = 1$ is slow, suggesting that in large but finite systems, where $C(0)$ has already converged to the separatrix value C_0^*, periodic motion as described in Fig.5 (D, E) can still be observed. However, as explained earlier, the stability analysis of stationary trajectories carried out in App.B suggests that such a periodic motion eventually loses its stability.

In summary, we have found two types of criticality, one SG like (type-II), and the other ferromagnetic like (type-I). All across the SG phase the system exhibits chaotic behavior in the thermodynamic limit, while in finite networks fixed points and periodic oscillations may emerge, especially close to the transition line.

B. Switching on fluctuations: Noisy dynamics ($\sigma \neq 0$) with uncorrelated interactions ($\gamma = 0$)

In this section, we analyze the effect of additional sources of external variability, particularly the presence of an external noise (i.e., $\sigma \neq 0$), on the firing-rate model for uncorrelated networks ($\gamma = 0$). In this case, there cannot be any fixed-point solution, as the rates $x_i(t)$ fluctuate stochastically. Non-fixed point steady states are characterised by the same magnetization M as in the noiseless dynamics, given by Eq.(22), while the equation for the correlator needs to be modified to (see SM, Sec. S.V A)

$$\partial_\tau^2 C = -\frac{\partial V(C|C(0), M)}{\partial C} - 2\sigma^2 \delta(\tau). \tag{34}$$

Integrating over $\tau \in [0, \epsilon]$, with $\epsilon \ll 1$ leads to

$$\dot{C}(\epsilon) = \dot{C}(0) - \sigma^2 + \mathcal{O}(\epsilon) \tag{35}$$

and recalling that $C(\tau) = C(-\tau)$ implies $\dot{C}(0) = 0$, one gets for $\epsilon \to 0^+$ that the initial velocity is $\dot{C}(0^+) = -\sigma^2$, as previously found in[50]. From now on, for the sake of simplicity, we focus on the case $M = 0$.

Let us remark that, as noticed earlier, $V'(C(0)|C(0), 0) < 0$ for $C(0) > q$, so that this led to un-physical solutions in the *noiseless* case, where $\dot{C}(0) = 0$. However, the situation is different in the presence of noise; given that the initial velocity is *negative*, a physical solution can *still* be obtained if the total energy is equal to zero, which corresponds to the separatrix curve, i.e. asymptotic motion towards $C = 0$ (see Fig.8(B)). This occurs for the initial condition $C(0) = C_\sigma^*$ such that

$$V(C_\sigma^*|C_\sigma^*, 0) = -\frac{1}{2}\sigma^4. \tag{36}$$

On the other hand, *any* $C(0) \leq q$ is physically plausible as it leads to bounded motion. To ascertain the value of $C(0)$ that is dynamically selected by the system, we plot in Fig.8(C) the distribution $P(C_0)$, defined in Eq.(30), computed from $S = 1000$ simulations of the microscopic dynamics, versus $1/gJ$, as a heat map, as well as the value of C_σ^* and q, as defined in Eq.(36) and Eq.(17),

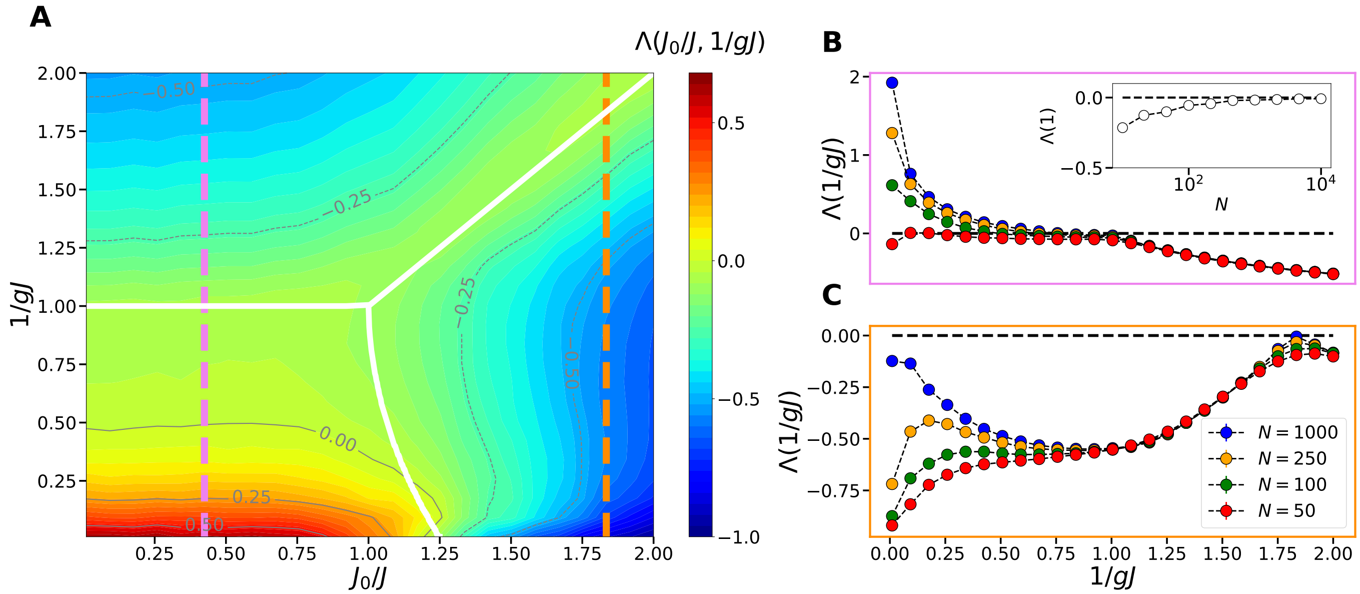

FIG. 7. **Panel (A)**: Largest Lyapunov exponent (LLE) Λ versus J_0/J, $1/gJ$ as mesured in simulations for the **uncorrelated** ($\gamma = 0$) and **noiseless** ($\sigma^2 = 0$) case for networks of size $N = 100$ and $S = 1000$ realizations. Chaotic behavior emerges below the isocline 0.00. **Panel (B, C)**: Λ versus $1/gJ$ for different values of N, as shown in the legend, and 2 different values of J_0/J, as indicated by the dashed lines on the left panel ((B) and (C) panels correspond to the left and right lines, respectively). At the smaller value of J_0/J (panel (B)) there exists a critical value $1/g^*J$ below which the LLE becomes positive; such a value tends to 1 as N increases as show in the inset; in particular, $\Lambda(1/gJ = 1)$ as a function of N converges asymptotically to 0. For the larger value of J_0/J (panel (C)) Λ is negative for all $1/gJ$ and remains so by increasing network size; thus, there is no chaos in the ferromagnetic phase.

respectively. Results show that $P(C_0)$ concentrates on the curve $C(0) = C^*_\sigma$. As we explained above, while for $C(0) > q$ this is the *only physical* solution, for $C(0) \leq q$, there are in principle many possible solutions. A stability analysis of steady-state solutions (see App. B) shows however that such solutions are all unstable, except for $C(0) = C^*_\sigma$, which is *marginally* stable. Then, the system selects the one laying on the separatrix curve, which delimits different possible (unstable) motions. As any fluctuation leads to an instability, chaotic behaviour is expected to emerge in single instances for $C^*_\sigma < q$. The critical line $C^*_\sigma = q$ is thus predicted to mark the transition to chaos. In Fig.9(A) we plot q and C^*_σ versus $1/gJ$, for different values of σ. The intersection between C^*_σ and q, obtained from

$$C^*_\sigma = \int \mathcal{D}\psi \, \tanh^2(gJ\sqrt{C^*_\sigma}\psi) \tag{37}$$

gives a curve in the $(\sigma^2, 1/gJ)$-plane plotted in Fig.9(B). A similar condition to Eq.(37) has been derived in[50] for the model originally defined by SCS in[29]. Let us remark that the variant of the model we consider here has a narrower chaotic region than the original model, in spite of the fact that their behaviour is identical in the absence of noise. This observation can be rationalised by a simple argument (see App. A) which shows that in our variant of the model the noise strength σ^2 is effectively amplified by a factor $(gJ)^2$, which is larger than 1, in the spin glass region. In the inset of Fig.9(B) we show the equivalent curve g^*J as a function of $\sigma\, g^*J$, for fixed J, recovering precisely the result obtained in[50].

The emergence of chaos in the noisy dynamics is confirmed by numerical analysis of the LLE, shown in Fig.10. For $J_0/J = 0.5$, the LLE Λ is plotted as a function of $1/gJ$ for different values of σ^2 and fixed $N = 1000$. The critical values $1/g^*J$ at which the Λ becomes positive, i.e. $\Lambda(1/g^*J) = 0$, are plotted in the inset, which are in agreement with the critical line defined in Eq.(37) (solid, red line).

Thus, the size of the chaotic phase is reduced by the presence of external noise, so that the boundary of the chaotic phase is shifted towards larger coupling values, in agreement with previously reported results.

C. Switching on correlations ($\gamma \neq 0$)

In this section, we analyse the dynamics when interactions are correlated ($\gamma \neq 0$). Any degree of correlations introduces a so-called "retarded" self-interaction in the equation for the effective single-neuron Eq.(10) i.e. a term non-local in time, which makes the dynamics non-Markovian and the analysis considerably harder. For this reason, here, we restrict our analysis to fixed-point solutions of the noiseless dynamics ($\sigma = 0$).

In the fixed-point regime, the response function is

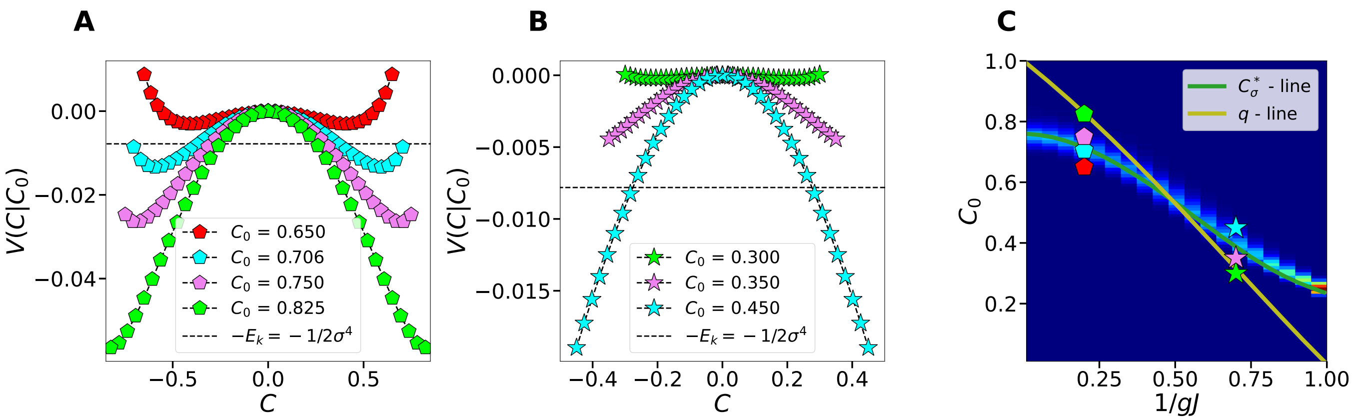

FIG. 8. Analysis of the motion in the effective potential $V(C|C(0), M)$ for the **uncorrelated** ($\gamma = 0$) and **noisy** ($\sigma^2 \neq 0$) case, for $M = 0$ (spin-glass phase, with $J_0/J = 0.5$). **Panels (A, B)**: Potential $V(C|C_0)$ as a function of C for fixed $1/gJ = 0.2$ and $1/gJ = 0.7$, respectively; plotted in the range $C \in [-C(0), C(0)]$ for different values of C_0 (as shown in the legend, with a color code). The dashed black line shows the negative of the initial kinetic energy, $-1/2\,\sigma^4$, arising from the noise. When this value is equal to the initial potential energy, the total energy is zero, corresponding to motion on the separatrix (blue curve in A). **Panel (C)**: Heat map of the probability distribution function (PDF) $P(C_0)$ of finding a given value of $C(0)$ in the SG phase, measured from $S = 1000$ simulations of the microscopic dynamics averaged over a time window $t_m = 2000$ for system size $N = 100$. Stars and pentagons show the values of $1/gJ$ and C_0 used in panel (B) and (C), respectively. Solid lines show the values of $C(0)$ corresponding to C_σ^* (green) as defined in Eq.(37) and q (yellow). The intersection between both lines defines the critical value $1/g^*J$ at which chaos emerges in the infinite-size limit (see Sec. B).

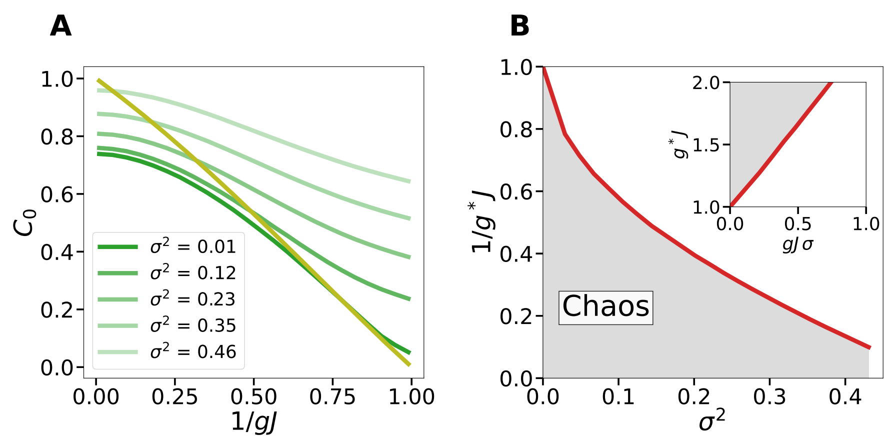

FIG. 9. Theoretical prediction of the critical line for the **uncorrelated** ($\gamma = 0$) and **noisy** system ($\sigma^2 \neq 0$). **Panel (A)**: C_σ^*, as defined in Eq.(36), as a function of $1/gJ$ for different values of σ^2 (green lines) plotted together with the solution of Eq.(37) as a function of $1/gJ$ (yellow line). The intersection between each green line and the yellow line defines the critical value $1/g^*J$ at which chaos emerges in the infinite-size limit for each value of σ. **Panel (B)**: Critical value $1/g^*J$ as a function of σ^2. As the noise strength σ^2 increases, the chaotic region delimited by $1/g^*J$ (grey region) shrinks, eventually disappearing when the noise amplitude is sufficiently large. In the inset, we plot the critical value g^*J as a function of the "scaled" $\sigma' = \sigma\, gJ$, where our model becomes equivalent to the SCS (see App. A). Results are consistent with the critical line derived in[50].

time-translation invariant $R(t,t') = R(t-t')$ and $C(t,t')$ becomes independent of t, t', so that it can be written as $q = C(t,t')$. As before, each realization of $\phi(t)$ becomes a static Gaussian random variable with zero mean and variance g^2J^2q. Setting $\phi = gJ\sqrt{q}\psi$, where ψ is a zero-average random variable with unit variance, the fixed point of Eq.(10) satisfies, for each realization of ψ,

$$x(\psi) = \tanh[J_0 gM + \gamma J^2 g^2 \chi x(\psi) + gJ\sqrt{q}\psi] \tag{38}$$

where $\chi = \int_0^\infty d\tau R(\tau)$ is the integrated response, which is found from Eq.(14) as

$$\chi = \left\langle \frac{\partial x(\phi)}{\partial \phi} \right\rangle \equiv \frac{1}{gJ\sqrt{q}} \left\langle \frac{\partial x(\psi)}{\partial \psi} \right\rangle . \tag{39}$$

Averaging Eq.(38) over ψ, we obtain

$$\begin{aligned} M &= \langle x(\psi) \rangle \qquad (40) \\ &= \int D\psi \tanh[J_0 gM + \gamma J^2 g^2 \chi x(\psi) + gJ\sqrt{q}\psi], \end{aligned}$$

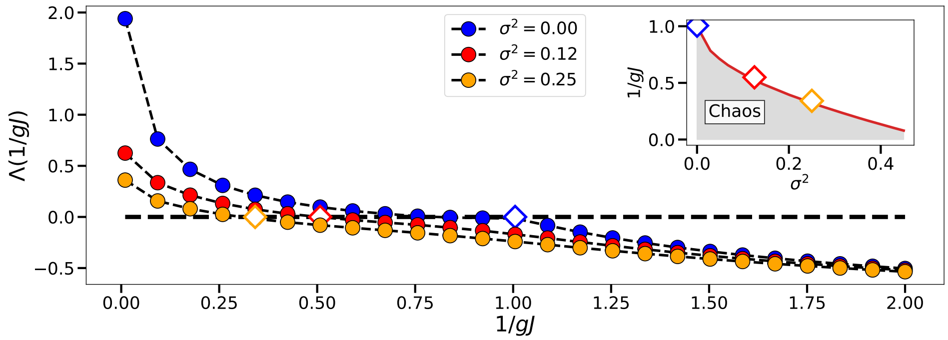

FIG. 10. For the **uncorrelated** ($\gamma = 0$) system, the largest Lyapunov exponent Λ, obtained from numerical simulations, is shown as a function of $1/gJ$, for $J_0/J = 0.5$ and different noise levels $\sigma^2 = 0, 0.12$ and 0.25, as shown in the legend. Results are averaged over $S = 100$ realizations and system size $N = 1000$. In the inset, we reproduce Fig.9(B), adding the value $1/g^*J$ at which Λ becomes positive (white diamonds).

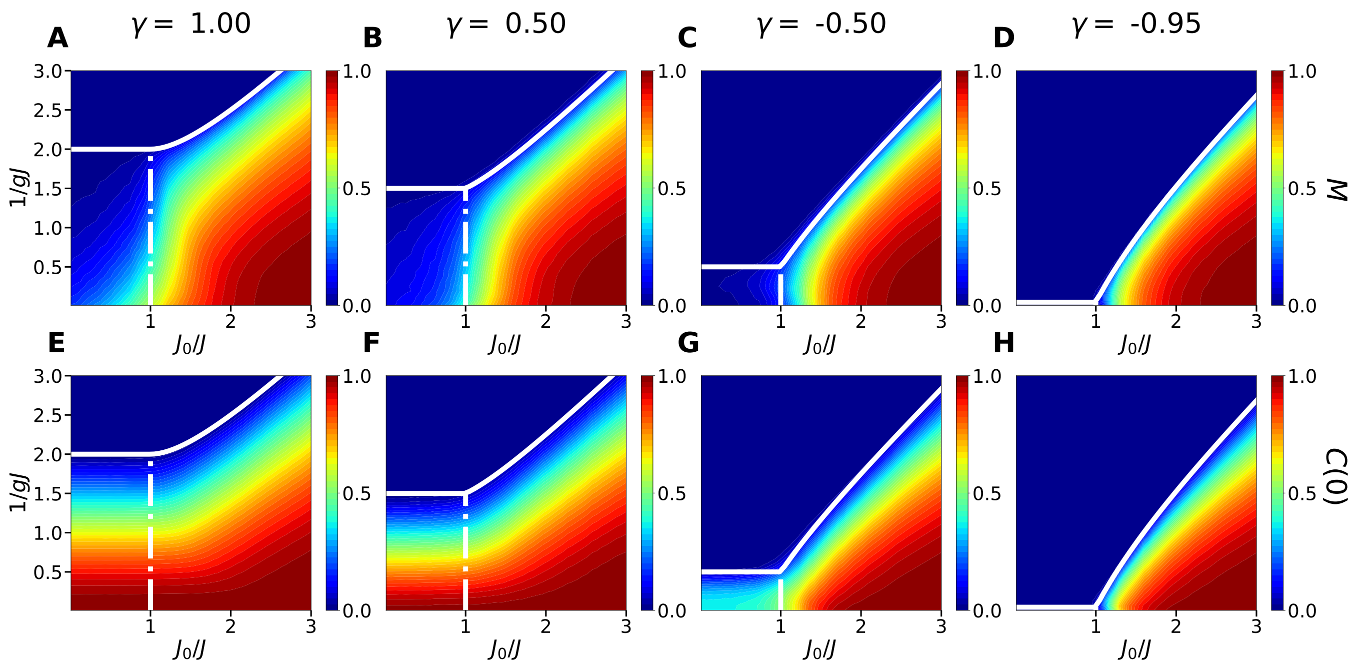

FIG. 11. Phase diagram emerging from simulations of networks with **correlated** couplings ($\gamma \neq 0$) and **noiseless** dynamics ($\sigma^2 = 0$). **Panel (A, B, C, D)**: Heat map of the time-averaged mean activity $\hat{M}$ for $\gamma = 1, 0.5, -0.5$ and -0.95, respectively. **Panels (E, F, G, H)**: Heat map of the time-averaged mean-squared activity $\hat{C}(0)$ for $\gamma = 1, 0.5, -0.5$ and -0.95, respectively. Solid, white lines show the theoretical prediction Eq.(42), while dotted, white lines show the curve $J_0/J = 1$, for visual aid. Each panel has been obtained integrating the microscopic dynamics for a system size $N = 100$ and averaging over $S = 1000$ different realizations.

and similarly

$$q = \langle x^2(\psi)\rangle = \int D\psi \tanh^2[J_0 g M + \gamma J^2 g^2 \chi x(\psi) + gJ\sqrt{q}\psi]. \tag{41}$$

As before, for $g = 0$ the system is in the paramagnetic phase $M = 0$, $q = 0$ and we expect this solution to remain stable below a critical value of g. However, in contrast with the case $\gamma = 0$, the equations for the moments M and q do not close, as they retain a dependence on the realizations x of the stochastic process. Nevertheless, progress can be made close to the paramagnetic instability, where $\tanh(x)$ can be linearised and equation closure can be achieved. In App. C we show that the critical line where the paramagnetic phase becomes unstable can be calculated explicitly as

$$\frac{1}{gJ} = \max\left(\gamma + 1, \frac{J_0}{J} + \gamma\frac{J}{J_0}\right) \tag{42}$$

Eq.(42) retrieves the line Eq.(4) for uncorrelated coupling ($\gamma = 0$) and Eq.(5) for reciprocal interactions ($\gamma = 1$), and it is consistent with results from random matrix theory. In particular, the first term corresponds to the largest eigenvalue, as derived in[40], while the second term recovers the expression for the outlier eigenvalue in matrices with a non-vanishing mean, derived in[41]. This underscores the versatility and significance of the derived expression across different analytical contexts. Also, as noted in[64], the largest eigenvalue of the bulk and the outlier are each given by the sum of their values at $\gamma = 0$ and a term which is proportional to γ. In the context of our analysis, this term can be rationalised as the additional contribution that M and q receive from the susceptibility (i.e. the integrated response), around the instability line. This relation shows that positively correlated interactions ($\gamma > 0$) enlarge the regions of ferromagnetic and spin-glass order, with respect to the case of uncorrelated interactions ($\gamma = 0$), while negatively correlated interactions ($\gamma < 0$) shrink the extension of the ordered phases, with the spin-glass region disappearing at $\gamma = -1$.

Finally, note that, owing to the non-linear and non-closed nature of equations, analyses away from criticality cannot be carried out exactly. Thus, we resort to numerical simulations.

In Fig.11 we show a heat map of the time averaged $\hat{M}$ and $\hat{C}(0)$ (computed from numerical simulations) in the parameter space $J_0/J, 1/gJ$, together with the theoretically determined critical line Eq.(42), for different values of γ (computed from the stability condition of fixed-point solutions). Observe that, even if non-fixed-point solutions are expected to appear in the ordered phase when interactions are non-symmetric (i.e. $\gamma < 1$), the theoretical lines obtained for fixed points are seen to capture well the actual phase-transitions for all values of γ. The figure clearly confirms the theoretical analyses: the spin-glass phase is enlarged for positively correlated couplings and progressively shrinks for negatively correlated ones (disappearing in the limit case $\gamma = -1$) and the theoretical lines correctly reproduce the actual phase transition in all cases.

Also, in Fig.12 we show results for the LLE as a function of the coupling strength ($1/gJ$), computed for different values of γ. The curves show that, for all values of γ, the exponents become positive below some critical value (marked with diamond symbol) that is consistent with the critical line $1/g_cJ = 1+\gamma$. Finite-size effects are quantified in the inset (for $\gamma = -0.15$). This shows that chaotic behaviour extends to the whole spin-glass region for all values of γ.

Some remarks are in order:

- The critical value (in terms of $1/gJ$) decreases as γ is reduced, so that it is maximal for $\gamma = 1$ (in agreement with the theoretical prediction).

- Smaller values of γ have larger LLEs in the limit of large coupling values (small $1/gJ$'s), so that, in this regime, the dynamics becomes more chaotic for anti-correlated couplings than for positively correlated ones.

- Indeed, as the value of γ approaches 1, the LLE becomes very close to 0 all across the spin-glass phase, so that, actually, the dynamics becomes marginally stable in such a limit. This last result resembles the recent observation of a phase of marginal stability in fully-correlated (i.e. symmetric) random networks in models for theoretical ecology[18]. Dynamics in such region can be regarded as "at the edge of chaos", as defined in other contexts see e.g.[11,65–67].

In summary, the introduction of correlations in the couplings quantitatively modifies the shape of the phase diagram with respect to the uncorrelated case: the spin-glass region is enlarged for positive correlations and shrinks for anticorrelated ones. On the other hand, the "strength" of chaos is larger for anticorrelations and tends to be reduced by positive correlations, leading to marginal stability in the limit of perfectly correlated couplings.

V. DISCUSSION AND CONCLUSIONS

In this study we have considered a simple neural network rate model with random Gaussian non-reciprocal interactions, having non-vanishing mean and possible correlations. We have analyzed the dynamics averaged over the network ensemble in the thermodynamic limit using a path integral formalism. These analytical studies have been complemented with extensive numerical simulations finite networks.

In general, much like in the physics of standard (reciprocal) disordered systems, fixed-point solutions are characterised by two order parameters, namely the mean (M) and the variance (q) of the neural activity. Thus, two different types of criticality emerge depending on whether the mean becomes non-zero (type-I) or not (type-II) at the transition, as the strength of the coupling is increased.

These criticalities correspond to the transition of the system from the paramagnetic phase to either a ferromagnetic (type-I) or spin-glass (type-II) phase, respectively.

Our analyses show that as soon as some degree of non-reciprocity is switched on —i.e., for any value of the coupling correlations, from nearly symmetric to anti-symmetric, $-1 < \gamma < 1$— there is a region, within the paramagnetic phase, where the network is reactive so that initial perturbations can be amplified before relaxing back to the fixed point solution. Moreover, for all values of the coupling correlations, a chaotic behavior emerges within the spin-glass phase ($M = 0$, $q \neq 0$). Furthermore, we have shown how the presence of correlations (i.e. some degree of reciprocity) in the couplings changes the phase diagram: negative correlations shrink the spin-glass phase (where chaotic dynamics emerges) while positive correlations enlarge it. On the other hand, negative correlations increase the strength of chaos, while positive

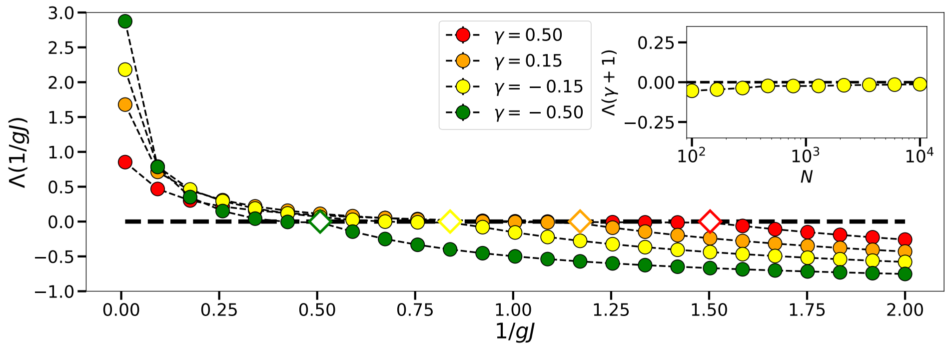

FIG. 12. For **correlated** ($\gamma \neq 0$) and **noiseless** dynamics ($\sigma^2 = 0$), largest Lyapunov exponent, Λ, obtained from simulations of the system, with size $N = 1000$, averaged over $S = 100$ realizations, for $J_0/J = 0.5$ and different values of γ, as shown in the legend. The point at which Λ becomes positive is depicted as a white diamond. The inset shows the value of Λ at $1/gJ = \gamma + 1$, for $\gamma = 0.15$, as a function of N.

correlations reduce it, with chaos disappearing for symmetric couplings. In this case, equilibrium is attained, and the whole spin-glass phase exhibits marginal stability, similar to what is observed in[18]. We have demonstrated that the extent of the chaotic phase diminishes with the introduction of external noise, indicating that noise tends to suppress chaos, consistent with findings from previous studies[50].

Chaotic phases observed in networks characterized by non-reciprocal couplings represent an intrinsic non-equilibrium phenomenon, yet they exhibit intriguing analogies with equilibrium spin-glass phases. For instance, our analysis demonstrates that within the chaotic phase, the dynamical equation governing the global two-time correlation function permits the existence of multiple steady states, encompassing fixed points and periodic orbits. However, our analyses reveal that the system *dynamically* selects the steady state that corresponds to motion along the *separatrix* curve, which delimits the basins of attractions of different types of solutions. This behavior is reminiscent of equilibrium systems in spin-glass (fRSB) phases, where a multitude of steady states emerges and the system is observed to select *marginally stable* ones, i.e. saddles in the free-energy landscape, that are linked together by flat directions. Our analyses also suggest that chaotic motion is the manifestation, at the level of *single network instances*, of an ensemble-averaged dynamics that lies on the separatrix curve delimiting different possible steady states. Such a motion is not time-translation invariant (TTI), similarly to ageing dynamics in spin-glass phases.

This last observation led us to propose a method for identifying the initiation of chaotic behavior. This method relies on a linear stability analysis of the steady-state solutions with respect to perturbations that disrupt time translation invariance. Our method is consistent with the two-replica approach described in[50,57], but it is considerably simpler, and it shows that chaotic behaviour emerges whenever the equation for the global correlation function allows for multiple steady-states.

The sensitive dependence on initial conditions in the chaotic phase implies that two "replicas" - two copies of the system with the same disorder but initialized with different configurations - exhibit distinct dynamical behaviors, resembling replicas of an equilibrium system ending up in different states. Furthermore, we find that while the global correlator exhibits multiple steady states in the chaotic phase, the presence of both a signal (i.e., a non-vanishing mean connectivity) and noise drives the system to a phase where only one steady state exists. This, again, mirrors what happens in equilibrium settings, where signal and thermal noise are known to induce transitions from the spin-glass phase to the ferromagnetic and paramagnetic phase respectively.

A theoretical prediction for the transition line between the spin-glass and the ferromagnetic region, for general values of the coupling asymmetry as well as a derivation of the asymptotic behaviour of the order parameters near criticality are currently missing. In particular, as we have seen, when interactions are not uncorrelated (or fully asymmetric), the equations for the time-dependent moments of the stochastic process do not close. This prevents an exact analysis away from the paramagnetic instability, to address the previous questions. However, one may be able to use closure schemes (e.g. Gaussian closure) as an approximation to further characterize the phase diagram of fixed-point solutions. In addition, within such approximation schemes, one might be able to obtain a closed equation for the two-time correlation at stationarity, which can be formulated as a gradient-descent on a potential. This approach can extend the analysis conducted for fully asymmetric couplings to interactions with arbitrary asymmetry. Another outlook could involve adapting the methodologies outlined in[68,69] to either numerically sample or analytically calculate fluctuations in the largest Lyapunov exponent. This approach could help identify model parameters where such fluctuations become unusually large, indicating the onset of chaos.

Finally, it would be important to further investigate whether chaotic dynamics and its links with spin-glass phases survive when different couplings, other than Gaussian, are chosen. For example, for applications in neuroscience, it would be interesting to carry out a similar analysis for couplings which satisfy Dale's rule[37] or are non-Gaussian[70], whereas the choice of *sparse* couplings may be relevant to applications in biology (e.g. gene regulatory networks[11,71]) and theoretical ecology (e.g. Lotka-Volterra models[18,20,43]).

Acknowledgments: We acknowledge the Spanish Ministry and Agencia Estatal de investigación (AEI) through Project of I+D+i Ref. PID2020-113681GB-I00, funded by MICIN/AEI/10.13039/501100011033 for financial support. We also acknowledge the support from the Consejería de Conocimiento, Investigación Universidad, Junta de Andalucía and European Regional Development Fund, Project reference P20-00173. AA wishes to thank Carlos-I Institute of Theoretical and Computational Physics at the University of Granada, for the kind hospitality.

References

[1] M. Mézard, G. Parisi, and M. A. Virasoro, *Spin glass theory and beyond: An Introduction to the Replica Method and Its Applications*, Vol. 9 (World Scientific Publishing Company, 1987).

[2] T. Castellani and A. Cavagna, "Spin-glass theory for pedestrians," Journal of Statistical Mechanics: Theory and Experiment **2005**, P05012 (2005).

[3] H. Nishimori, *Statistical physics of spin glasses and information processing: an introduction*, 111 (Clarendon Press, 2001).

[4] P. Charbonneau, E. Marinari, G. Parisi, F. Ricci-tersenghi, G. Sicuro, F. Zamponi, and M. Mezard, *Spin Glass Theory and Far Beyond: Replica Symmetry Breaking after 40 Years* (World Scientific, 2023).

[5] T. Aspelmeier, A. J. Bray, and M. A. Moore, "Complexity of ising spin glasses," Phys. Rev. Lett. **92**, 087203 (2004).

[6] A. Cavagna, I. Giardina, and G. Parisi, "Numerical study of metastable states in ising spin glasses," Phys. Rev. Lett. **92**, 120603 (2004).

[7] A. Annibale, G. Gualdi, and A. Cavagna, "Coexistence of supersymmetric and supersymmetry-breaking states in spherical spin-glasses," Journal of Physics A: Mathematical and General **37**, 11311 (2004).

[8] M. Müller and M. Wyart, "Marginal stability in structural, spin and electron glasses," Annu. Rev. Condens. Matter Phys. **6**, 177–200 (2015).

[9] A. V. Herz and J. J. Hopfield, "Earthquake cycles and neural reverberations: Collective oscillations in systems with pulse-coupled threshold elements," Phys. Rev. Lett. **75**, 1222–1225 (1995).

[10] M. M. D. Challet, A. Chessa and Y.-C. Zhang, "From minority games to real markets," Quantitative Finance **1**, 168–176 (2001).

[11] D. Stokić, R. Hanel, and S. Thurner, "Inflation of the edge of chaos in a simple model of gene interaction networks," Phys. Rev. E **77**, 061917 (2008).

[12] J. M. Beggs and N. Timme, "Being critical of criticality in the brain," Frontiers Physiol. **3** (2012).

[13] T. Mora and W. Bialek, "Are biological systems poised at criticality?" J. Stat. Phys. **144** (2011).

[14] M. A. Muñoz, "Colloquium: Criticality and dynamical scaling in living systems," Reviews of Modern Physics **90**, 031001 (2018).

[15] P. Moretti and M. A. Muñoz, "Griffiths phases and the stretching of criticality in brain networks," Nature communications **4**, 1–10 (2013).

[16] M. Martinello, J. Hidalgo, A. Maritan, S. Di Santo, D. Plenz, and M. A. Muñoz, "Neutral theory and scale-free neural dynamics," Phys. Rev. X **7**, 041071 (2017).

[17] S. di Santo, P. Villegas, R. Burioni, and M. A. Muñoz, "Landau–ginzburg theory of cortex dynamics: Scale-free avalanches emerge at the edge of synchronization," Proceedings of the National Academy of Sciences **115**, E1356–E1365 (2018).

[18] G. Biroli, G. Bunin, and C. Cammarota, "Marginally stable equilibria in critical ecosystems," New Journal of Physics **20**, 083051 (2018).

[19] A. Altieri and S. Franz, "Constraint satisfaction mechanisms for marginal stability and criticality in large ecosystems," Physical Review E **99**, 010401 (2019).

[20] A. Altieri, F. Roy, C. Cammarota, and G. Biroli, "Properties of equilibria and glassy phases of the random Lotka-Volterra model with demographic noise," Phys. Rev. Lett. **126**, 258301 (2021).

[21] G. Bunin, "Ecological communities with Lotka-Volterra dynamics," Phys. Rev. E **95**, 042414 (2017).

[22] T. M. Pham and K. Kaneko, "Double-replica theory for evolution of genotype-phenotype interrelationship," Phys. Rev. Research **5**, 023049 (2023).

[23] L. Correale, M. Leone, A. Pagnani, M. Weigt, and R. Zecchina, "The computational core and fixed point organization in boolean networks," Journal of Statistical Mechanics: Theory and Experiment **2006**, P03002 (2006).

[24] Y. V. Fyodorov and B. A. Khoruzhenko, "Nonlinear analogue of the may-wigner instability transition," Proc. Natl. Acad. Sci. **113**, 6827–6832 (2016).

[25] S. Hwang, V. Folli, E. Lanza, G. Parisi, G. Ruocco, and F. Zamponi, "On the number of limit cycles in asymmetric neural networks," Journal of Statistical Mechanics: Theory and Experiment **2019**, 053402 (2019).

[26] S. B. Fedeli, Y. V. Fyodorov, and J. Ipsen, "Nonlinearity-generated resilience in large complex systems," Phys. Rev. E **103**, 022201 (2021).

[27] B. Lacroix-A-Chez-Toine and Y. V. Fyodorov, "Counting equilibria in a random non-gradient dynamics with heterogeneous relaxation rates," Journal of Physics A: Mathematical and Theoretical **55**, 144001 (2022).

[28] V. Ros, F. Roy, G. Biroli, G. Bunin, and A. M. Turner, "Generalized Lotka-Volterra equations with random, nonreciprocal interactions: The typical number of equilibria," Phys. Rev. Lett. **130**, 257401 (2023).

[29] H. Sompolinsky, A. Crisanti, and H.-J. Sommers, "Chaos in random neural networks," Phys. Rev. Lett. **61**, 259 (1988).

[30] I. Ginzburg and H. Sompolinsky, "Theory of correlations in stochastic neural networks," Phys. Rev. E **50**, 3171–3191 (1994).

[31] M. Fruchart, R. Hanai, P. B. Littlewood, and V. Vitelli, "Non-reciprocal phase transitions," Nature **592**, 363–369 (2021).

[32] G. Wainrib and J. Touboul, "Topological and dynamical complexity of random neural networks," Phys. Rev. Lett. **110**, 118101 (2013).

[33] P. Dayan and L. F. Abbott, *Theoretical Neuroscience: Computational and Mathematical Modeling of Neural Systems* (Cambridge, MIT Press, USA, 2006) Chap. 7, Network Models.

[34] P. Van Mieghem, *Graph spectra for complex networks* (Cambridge University Press, 2010).

[35] S. N. Dorogovtsev, A. V. Goltsev, J. F. Mendes, and A. N. Samukhin, "Spectra of complex networks," Phys. Rev. E **68**, 046109 (2003).

[36] T. Tao, "Outliers in the spectrum of iid matrices with bounded rank perturbations," Probab. Theory Relat. Fields **155**, 231–263 (2013).

[37] K. Rajan and L. Abbott, "Eigenvalue spectra of random matrices for neural networks," Phys. Rev. Lett. **97**, 188104 (2006).

[38] A. Knowles and J. Yin, "The Isotropic Semicircle Law and Deformation of Wigner Matrices," Communications on Pure and Applied Mathematics **66**, 1663–1749 (2013).

[39]A. Knowles and J. Yin, "The outliers of a deformed Wigner matrix," The Annals of Probability **42** (2014), 10.1214/13-AOP855.

[40]H. J. Sommers, A. Crisanti, H. Sompolinsky, and Y. Stein, "Spectrum of Large Random Asymmetric Matrices," Phys. Rev. Lett. **60**, 1895–1898 (1988).

[41]S. O'Rourke and D. Renfrew, "Low rank perturbations of large elliptic random matrices," Electronic Journal of Probability **19**, 1–65 (2014), arXiv:1309.5326 [math-ph].

[42]D. Dahmen, S. Grün, M. Diesmann, and M. Helias, "Second type of criticality in the brain uncovers rich multiple-neuron dynamics," Proc. Natl. Acad. Sci. **116**, 13051–13060 (2019).

[43]E. R. Garcia, M. J. Crumpton, and T. Galla, "Niche overlap and hopfield-like interactions in generalized random Lotka-Volterra systems," Phys. Rev. E **108**, 034120 (2023).

[44]M. G. Neubert and H. Caswell, "Alternatives to resilience for measuring the responses of ecological systems to perturbations," Ecology **78**, 653–665 (1997).

[45]S. Tang and S. Allesina, "Reactivity and stability of large ecosystems," Frontiers in Ecology and Evolution **2**, 21 (2014).

[46]G. Yan, N. D. Martinez, and Y.-Y. Liu, "Degree heterogeneity and stability of ecological networks," Journal of the Royal Society Interface **14**, 20170189 (2017).

[47]F. Caravelli and P. P. Staniczenko, "Bounds on transient instability for complex ecosystems," PLoS One **11**, e0157876 (2016).

[48]B. K. Murphy and K. D. Miller, "Balanced amplification: a new mechanism of selective amplification of neural activity patterns," Neuron **61**, 635–648 (2009).

[49]S. Di Santo, P. Villegas, R. Burioni, and M. A. Muñoz, "Non-normality, reactivity, and intrinsic stochasticity in neural dynamics: a non-equilibrium potential approach," Journal of Statistical Mechanics: Theory and Experiment **2018**, 073402 (2018).

[50]J. Schuecker, S. Goedeke, and M. Helias, "Optimal sequence memory in driven random networks," Phys. Rev. X **8**, 041029 (2018).

[51]J. Kadmon and H. Sompolinsky, "Transition to chaos in random neuronal networks," Phys. Rev. X **5**, 041030 (2015).

[52]K. Rajan, L. F. Abbott, and H. Sompolinsky, "Stimulus-dependent suppression of chaos in recurrent neural networks," Phys. Rev. E **82**, 011903 (2010).

[53]F. Mastrogiuseppe and S. Ostojic, "Intrinsically-generated fluctuating activity in excitatory-inhibitory networks," PLoS computational biology **13**, e1005498 (2017).

[54]P. C. Martin, E. D. Siggia, and H. A. Rose, "Statistical dynamics of classical systems," Phys. Rev. A **8**, 423–437 (1973).

[55]A. Coolen, "Chapter 15 statistical mechanics of recurrent neural networks ii — dynamics," in *Neuro-Informatics and Neural Modelling*, Handbook of Biological Physics, Vol. 4, edited by F. Moss and S. Gielen (North-Holland, 2001) pp. 619–684.

[56]J. P. L. Hatchett and A. C. C. Coolen, "Asymmetrically extremely dilute neural networks with langevin dynamics and unconventional results," Journal of Physics A: Mathematical and General **37**, 7199 (2004).

[57]A. Crisanti and H. Sompolinsky, "Path integral approach to random neural networks," Phys. Rev. E **98**, 062120 (2018).

[58]M. Helias and D. Dahmen, "Dynamic mean-field theory for random networks," in *Statistical Field Theory for Neural Networks* (Springer, 2020) pp. 95–126.

[59]M. Opper and S. Diederich, "Phase transition and $1/f$ noise in a game dynamical model," Phys. Rev. Lett. **69**, 1616–1619 (1992).

[60]L. Sidhom and T. Galla, "Ecological communities from random generalized Lotka-Volterra dynamics with nonlinear feedback," Phys. Rev. E **101**, 032101 (2020).

[61]D. Sherrington and S. Kirkpatrick, "Solvable Model of a Spin-Glass," Phys. Rev. Lett. **35**, 1792–1796 (1975).

[62]We use the "hat" notation for quantities measured in simulations, to distinguish them from their theoretical counterparts, as obtained from the path integral approach. In particular, single-realizations are denoted by a subscript s, e.g., $\hat{M}_s$, whereas averages over many realizations are denoted with $\hat{M}$.

[63]For an ergodic system, where time averages are equivalent to ensemble averages, such quantity should equate the ensemble-averaged correlator $C(\tau)$, in the thermodynamic limit, if the system is at stationarity.

[64]S. Cure and I. Neri, "Antagonistic interactions can stabilise fixed points in heterogeneous linear dynamical systems," SciPost Physics **14**, 093 (2023).

[65]R. Hanel, M. Pöchacker, and S. Thurner, "Living on the edge of chaos: minimally nonlinear models of genetic regulatory dynamics," Phil. Trans. R. Soc. A. **368**, 5583–5596 (2010).

[66]G. B. Morales, S. Di Santo, and M. A. Muñoz, "Quasiuniversal scaling in mouse-brain neuronal activity stems from edge-of-instability critical dynamics," Proceedings of the National Academy of Sciences **120**, e2208998120 (2023).

[67]G. B. Morales and M. A. Muñoz, "Optimal input representation in neural systems at the edge of chaos," Biology **10**, 702 (2021).

[68]T. Laffargue, K.-D. N. T. Lam, J. Kurchan, and J. Tailleur, "Large deviations of lyapunov exponents," Journal of Physics A: Mathematical and Theoretical **46**, 254002 (2013).

[69]T. Laffargue, P. Sollich, J. Tailleur, and F. van Wijland, "Large-scale fluctuations of the largest lyapunov exponent in diffusive systems," Europhysics Letters **110**, 10006 (2015).

[70]A. Wardak and P. Gong, "Extended anderson criticality in heavy-tailed neural networks," Phys. Rev. Lett. **129**, 048103 (2022).

[71]G. Torrisi, R. Kühn, and A. Annibale, "Percolation on the gene regulatory network," Journal of Statistical Mechanics: Theory and Experiment **2020**, 083501 (2020).

[72]R. Toral and P. Colet, *Stochastic numerical methods: an introduction for students and scientists* (John Wiley & Sons, 2014).

[73]J. P. Eckmann and D. Ruelle, "Ergodic theory of chaos and strange attractors," Reviews of Modern Physics **57**, 617–656 (1985).

[74]A. Pikovsky and A. Politi, *Lyapunov exponents: a tool to explore complex dynamics* (Cambridge University Press, Cambridge, 2016).

[75]G. Benettin, L. Galgani, A. Giorgilli, and J.-M. Strelcyn, "Lyapunov Characteristic Exponents for smooth dynamical systems and for hamiltonian systems; A method for computing all of them. Part 2: Numerical application," Meccanica **15**, 21–30 (1980).

[76]A. Wolf, J. B. Swift, H. L. Swinney, and J. A. Vastano, "Determining Lyapunov exponents from a time series," Physica D: Nonlinear Phenomena **16**, 285–317 (1985).

[77]J.-F. Arnoldi, A. Bideault, M. Loreau, and B. Haegeman, "How ecosystems recover from pulse perturbations: A theory of short-to long-term responses," Journal of theoretical biology **436**, 79–92 (2018).

APPENDICES

Appendix A: On the equivalence between our model and the classic one (SCS)

In this section we show that the model originally introduced in[29] can be mapped to the variant we introduce here, when interactions are uncorrelated and zero-averaged, upon suitably scaling the noise strength. Multiplying Eq.(1),

$$\dot{x}_i = -x_i + \tanh(g \sum_j J_{ij} x_j) + \xi_i, \tag{A1}$$

times $gJ_{\ell i}$ and summing over i, we have, upon defining $y_\ell = g \sum_i J_{\ell i} x_i$ and $\phi_\ell = g \sum_i J_{\ell i} \xi_i$

$$\dot{y}_\ell = -y_\ell + g \sum_i J_{\ell i} \tanh(y_i) + \phi_\ell \tag{A2}$$

where

$$\begin{aligned} \langle \phi_\ell(t) \phi_k(t') \rangle &= g^2 \sum_{ij} J_{\ell i} J_{kj} \langle \xi_i(t) \xi_j(t') \rangle = 2g^2\sigma^2 \sum_{ij} J_{\ell i} J_{kj} \delta_{ij} \delta(t-t') \\ &= 2g^2\sigma^2 \sum_i J_{\ell i} J_{ki} \delta(t-t') \end{aligned} \tag{A3}$$

For uncorrelated, zero-mean Gaussian interactions $J_{ij} \sim \mathcal{N}(0, J^2/N)$, we have

$$\langle \phi_\ell(t) \phi_k(t') \rangle = 2g^2\sigma^2 J^2 \delta_{k\ell} \delta(t-t'), \tag{A4}$$

hence the two models are fully equivalent when rescaling σ with gJ. If, however, the J_{ij}'s are correlated or non-zero averaged, then the two models are no longer equivalent.

Appendix B: Stability of steady-state solutions with uncorrelated interactions ($\gamma = 0$)

In this section we study the linear stability of non-fixed points steady-states solutions. Away from stationarity, we can write the equation of motion for the two-time correlator $C(t,s)$ as

$$(1+\partial_t)(1+\partial_s) C(t,s) = F(C(t,s), C(t,t), C(s,s), C(s,t), M(t), M(s)) \tag{B1}$$

where

$$F(C(t,s), C(t,t), C(s,s), M(t), M(s)) = \int \mathcal{D}_{\phi,\phi'}(t,s)\ \tanh[J_0 g M(t) + \phi] \tanh[J_0 g M(s) + \phi'] \tag{B2}$$

where the Gaussian kernel is defined as

$$\mathcal{D}_{\phi,\phi'}(t,s) = \frac{d\phi d\phi'}{2\pi g^2 J^2 \sqrt{\det \mathcal{M}(t,s)}} \exp\left(-\frac{\boldsymbol{\phi}^T \mathcal{M}(t,s)^{-1} \boldsymbol{\phi}}{2J^2 g^2} \right) \tag{B3}$$

and

$$\mathcal{M}(t,s) = \begin{pmatrix} C(t,t) & C(t,s) \\ C(s,t) & C(s,s) \end{pmatrix}$$

As noted above, in Sec. IV A andIV B, chaotic motion is not time translation invariant, as trajectories are highly sensitive to their initial conditions; i.e. even small initial perturbations can lead to vastly different outcomes as time progresses.

In what follows, we examine the stability of stationary trajectories under small perturbations $\delta(t,s)$ that break time-translation invariance. Recalling that stationary solutions are characterized by a constant first moment $M(t) = M$ and time-translation invariant correlator $C(t,s) = C(t-s)$, we can write

$$C(t,s) = C(\tau) + \epsilon \delta(t,s) \tag{B4}$$

$$C(t,t) = C(s,s) = C(0) \tag{B5}$$

$$M(t) = M \tag{B6}$$

where $\tau = t - s$, i.e. we consider a non-stationary regime where one-time quantities remain constant and two-time quantities break time-translation invariance —much as happens in glassy regimes.

Inserting Eqs.(B4), (B5) and (B6) in the equation for the two-time correlator $C(t, s)$, given by Eq.(B1), Taylor expanding the right hand side for small ϵ to linear order and using $C(\tau) = C(-\tau)$ and

$$F(C(\tau), C(0), C(0), C(-\tau), M, M) \equiv \Xi(C(\tau), C(0), M), \tag{B7}$$

we get (i) to $\mathcal{O}(\epsilon^0)$ terms, Eq.(23); and (ii), to $\mathcal{O}(\epsilon)$, the following equation for the deviations from stationarity

$$(1 + \partial_t)(1 + \partial_s)\delta(t, s) = \delta(t, s) \left. \frac{\partial \Xi(C, C(0), M)}{\partial C} \right|_{C(\tau)}. \tag{B8}$$

Following[50], we set $T = t + s$ and $\tau = t - s$ and denote $\delta(t, s) = K(T, \tau)$ to rewrite the above as

$$\left[(\partial_T + 1)^2 - \partial_\tau^2\right] K(T, \tau) = K(T, \tau)\, \Xi'(C(\tau), C(0), M) \tag{B9}$$

The above partial differential equation can be solved via separation of variables, i.e. by searching for a solution in the factorised form

$$K(T, \tau) = \psi(\tau) e^{\kappa T/2} \tag{B10}$$

Inserting this ansatz into Eq.(B9), a Schrödinger's equation for $\psi(\tau)$ is obtained

$$[-\partial_\tau^2 - V''(C(\tau)|C(0), M)]\psi(\tau) = \left[1 - (\frac{\kappa}{2} + 1)^2\right] \psi(\tau) \tag{B11}$$

with quantum mechanical potential $-V''(C|C(0), M)$. As observed in[50] there will be a set of allowed energies $E_0 < E_1 < E_2 \ldots$, with $E_n = 1 - (\frac{\kappa_n}{2} + 1)^2$, and associated eigenfunctions $\psi_n(\tau)$. A stationary solution $C(\tau)$ will be linearly stable if the perturbation $K(T, \tau)$ decays with T, i.e. if the largest value of κ, $\kappa_0 = -1 + \sqrt{1 - E_0}$, is negative. This requires the ground state energy E_0 to be positive.

It is also useful to note that, as pointed out in[50], Eq.(23) implies

$$[-\partial_\tau^2 - V''(C(\tau)|C(0), M)]\, \dot{C}(\tau) = 0, \tag{B12}$$

hence non-fixed point steady-state solutions $\dot{C}(\tau) \neq 0$, correspond —when they exist— to eigenfunctions with energy $E = 0$.

As for an eigenfunction to exist, the energy must be greater or equal than the quantum-mechanical potential $-V''(C|C(0), M)$; if the latter is positive, all the eigenfunctions, including the ground state, have positive energy, hence the motion is stable.

1. For $M \neq 0$, $V'(C|C(0), M)$ is strictly decreasing for any $-C(0) \leq C \leq C(0)$ and $0 < C(0) \leq q$, hence $V''(C|C(0), M) < 0$. This implies that for any $C(0) \leq q$, $E_n > 0\ \forall\ n$ and the only allowed solution of Eq.(B12) is the fixed-point solution $C(\tau) = q$ (non-trivial solutions with zero energy are not allowed). Furthermore, this must be stable, as $E_0 > 0$.

2. Conversely, for $M = 0$, the potential has at least one minimum, either at $C = 0$ or $C = \pm\bar{C}(C(0))$, for any value of $C(0) \leq q$, hence Eq.(B12) allows a non-trivial solution, for any $C(0) < q$, which is either a periodic orbit or the separatrix curve. These represent eigenfunctions with energy $E = 0$. Periodic solutions have multiple nodes (as $\dot{C}$ vanishes at every turning point), whereas the separatrix curve has precisely one node in the noiseless case (where $\dot{C}(0) = 0$) and no node in the noisy case (where $\dot{C}(0^+) = -\sigma^2$). As noted in[50], in the noiseless case $\dot{C}$ has at least one node, hence it cannot be the ground state, but it must correspond to one of the excited states $\psi_n(\tau)$ with $n \geq 1$, implying that the ground-state energy is $E_0 < 0$.

   Recalling that, in the noiseless case, steady-state solutions are physical only for $C(0) \leq q$, we have that *all* physical steady-state solutions are unstable in the noiseless case.

   On the other hand, in the presence of noise, solutions with $C(0) > q$ are allowed, *only* for $C(0)$ equating the separatrix value C^*_σ, which solves Eq.(36). Since this is the only physical solution, it must be stable for $C^*_\sigma > q$. Conversely, any $C(0) < q$ leads to a physical solution. As for the noiseless case, such solutions are all unstable, except the separatrix curve, which is *marginally* stable (as it has no node for $\sigma \neq 0$). However, as any fluctuation leads to an instability, chaotic behaviour is expected to emerge in single instances for $C^*_\sigma < q$. The critical line $C^*_\sigma = q$ is thus predicted to mark the transition to chaos.

Appendix C: Phase Diagram for $\gamma \neq 0$

In this Appendix we derive the phase diagram for the fixed-point solutions of Eq.(10), when interactions are correlated. We note that for $g = 0$, the solution of Eq.(41)-(42) is $M = 0$, $q = 0$. It is expected that $(M, q) = (0, 0)$ remains stable for g below a critical value g_c, where non-trivial solutions emerge. In this region, Eq.(38) reduces to

$$x(\psi) = \tanh(\gamma g^2 J^2 x(\psi)) \tag{C1}$$

so that $x(\psi)$ is deterministic. We have $x(\psi) = 0$ for $\gamma g^2 J^2 < 1$ — either $\gamma > 0$ and $(gJ)^{-1} > \sqrt{\gamma}$, or $\gamma < 0$. For $\gamma > 0$ and $(gJ)^{-1} < \sqrt{\gamma}$, two non-zero solutions emerge $\pm x^\star$, one positive and one negative. Since $x(\psi) = \pm x^\star$ implies $q \neq 0$, bifurcations in x imply bifurcations in q, hence we assume that x is small when q is small. To locate g_c, we expand Eqs.(41)–(42) for small M, q and $x(\psi)$. Starting with Eq.(41), we have

$$\begin{aligned} M &= \int D\psi[J_0 g M + \gamma J^2 g^2 \chi x(\psi) + gJ\sqrt{q}\psi] \\ &= (J_0 g + \gamma J^2 g^2 \chi) M \end{aligned} \tag{C2}$$

To make progress, we need an expression for χ. Setting $\phi = gJ\sqrt{q}\psi$ we can write Eq.(38) as

$$x(\phi) = \tanh[J_0 g M + \gamma J^2 g^2 \chi x(\phi) + \phi] \tag{C3}$$

Differentiating Eq. (C3) with respect to ϕ we obtain

$$\frac{\partial x}{\partial \phi} = \left[1 - \tanh^2(gJ_0 M + \gamma g^2 J^2 \chi x + \phi)\right] \left(\gamma g^2 J^2 \chi \frac{\partial x}{\partial \phi} + 1\right), \tag{C4}$$

and re-arranging

$$\frac{\partial x}{\partial \phi}\Big\{1 - \gamma g^2 J^2 \chi[1 - \tanh^2(gJ_0 M + \gamma g^2 J^2 \chi x + \phi)]\Big\} = 1 - \tanh^2(gJ_0 M + \gamma g^2 J^2 \chi x + \phi), \tag{C5}$$

so that, writing in terms of ψ, we have

$$\begin{aligned} &\frac{1}{gJ\sqrt{q}} \frac{\partial x}{\partial \psi}\Big\{1 - \gamma g^2 J^2 \chi[1 - \tanh^2(gJ_0 M + \gamma g^2 J^2 \chi x + gJ\sqrt{q}\psi)]\Big\} \\ &\qquad = 1 - \tanh^2(gJ_0 M + \gamma g^2 J^2 \chi x + gJ\sqrt{q}\psi) \end{aligned} \tag{C6}$$

Close to the transition line M, q and x are small. A leading-order expansion in these quantities gives

$$\frac{1}{gJ\sqrt{q}} \frac{\partial x}{\partial \psi}\Big\{1 - \gamma g^2 J^2 \chi\Big\} = 1. \tag{C7}$$

Finally, averaging over ψ and using Eq.(39) we get

$$\chi(1 - \gamma g^2 J^2 \chi) = 1 \tag{C8}$$

The physical solution is

$$\chi = \frac{1 - \sqrt{1 - 4\gamma g^2 J^2}}{2\gamma g^2 J^2} \tag{C9}$$

(as the other diverges when $g \to 0$). Substituting in Eq.(C2), we have that M bifurcates at

$$gJ_0 + \gamma g^2 J^2 \frac{1 - \sqrt{1 - 4\gamma g^2 J^2}}{2\gamma g^2 J^2} = 1 \tag{C10}$$

which gives

$$\frac{1}{gJ} = \frac{J_0}{J} + \gamma \frac{J}{J_0} \tag{C11}$$

Similarly, expanding the equation for q, Eq.(42), and setting $M = 0$ we obtain

$$q = \int \mathcal{D}\psi[J_0 gM + \gamma J^2 g^2 \chi x(\psi) + gJ\sqrt{q}\psi]^2 = \gamma^2 J^4 g^4 \chi^2 q + g^2 J^2 q + 2\gamma(gJ)^3 \chi\sqrt{q} \int \mathcal{D}\psi x(\psi)\psi$$
$$= (\gamma^2 J^4 g^4 \chi^2 + g^2 J^2 + 2\gamma(gJ)^4 \chi^2) q \tag{C12}$$

where we have integrated by parts

$$\int \mathcal{D}\psi x(\psi)\psi = \int \frac{d\psi}{\sqrt{2\pi}} \Big(- \frac{\partial}{\partial\phi} e^{-\psi^2/2} \Big) x(\psi) = \int \frac{d\psi}{\sqrt{2\pi}} e^{-\psi^2/2} \frac{\partial}{\partial\psi} x(\psi) = \Big\langle \frac{\partial x}{\partial\psi} \Big\rangle = gJ\sqrt{q}\chi. \tag{C13}$$

Substituting Eq.(C9) in Eq.(C12) we see that bifurcations in q occur at

$$1 = \frac{\gamma + 2}{2\gamma}(1 - \sqrt{1 - 4\gamma g^2 J^2} - 2\gamma g^2 J^2) + g^2 J^2 \tag{C14}$$

which can be simplified to

$$\frac{2}{g^4 J^4} - (2\gamma^2 + 3\gamma + 2)\frac{1}{g^2 J^2} - \gamma(\gamma + 1)^2 = 0. \tag{C15}$$

As the physical solution must be positive, it follows that

$$\frac{1}{gJ} = \frac{1}{2}\sqrt{(2\gamma^2 + 3\gamma + 2) \pm \sqrt{(2\gamma^2 + 3\gamma + 2)^2 + 8\gamma(\gamma + 1)^2}}. \tag{C16}$$

With little algebra, the expression above can be simplified to

$$\frac{1}{gJ} = \frac{1}{2}\sqrt{2 + \gamma(2\gamma + 3) \pm |2\gamma^2 + 5\gamma + 2|} \equiv a(\gamma). \tag{C17}$$

As $2\gamma^2 + 5\gamma + 2 \geq 0$ for $\gamma \geq -1/2$, we have

$$a(\gamma) = \begin{cases} \frac{1}{2}\sqrt{2 + \gamma(2\gamma + 3) \pm (2\gamma^2 + 5\gamma + 2)} & \gamma \geq -1/2 \\ \frac{1}{2}\sqrt{2 + \gamma(2\gamma + 3) \mp (2\gamma^2 + 5\gamma + 2)} & \gamma < -1/2 \end{cases} \tag{C18}$$

hence there are two possible solutions, $a_+(\gamma) = 1 + \gamma$ and $a_-(\gamma) = \sqrt{-\gamma/2}$, the latter existing only for $\gamma < 0$. As for $\gamma = -1$, all the eigenvalues of the interaction matrix $\mathbf{J}$ are purely imaginary, no (non-trivial) fixed-point solution are expected to bifurcate from $\mathbf{x} = 0$, as bifurcating solutions must be purely oscillatory. Hence, it is expected that $a(-1) = 0$. This suggests that the solution $a_+(\gamma)$ is the physical one for any $\gamma \in [-1, 1]$. Combining Eq.(C11) with the result $a(\gamma) = 1 + \gamma$, we obtain the critical line where the paramagnetic phase becomes unstable given in Eq.(42).

Appendix D: Numerical procedure

1. Computation of trajectories

In simulations, trajectories of Eq.(1) are computed numerically by a simple Midpoint Runge-Kutta method (see, for instance,[72]). The time step is fixed $h = 0.1$, except for the calculation of the LLE for which $h = 0.01$ because of the numerical sensitivity of the Bennetin-Wolf procedure. In order to avoid the transient regime, trajectories are integrated up to $t_{max} = 2000$ units of time. The initial step $\mathbf{x}_0$ and the matrix $\mathbf{J}$ are selected randomly for each instance of the simulation. In particular, each pair (J_{ij}, J_{ji}), for $1 \leq i < j \leq N$, is generated following a multivariate Gaussian distribution with average $\boldsymbol{\mu}$ and covariance matrix $\boldsymbol{\Sigma}$, as defined in (S13), respectively. The diagonal elements, J_{ii}, are each obtained from a Gaussian distribution with average J_0/N and variance J^2/N.

2. Shape of the potential $V(C|C(0), M)$

In order to numerically compute $V(C|C(0), M)$, we simplify the function $\Xi(C, C(0), M)$, defined in Eq.(24), as follows. The Gaussian kernel, Eq.(25), is divided into two parts using the conditional probability formula of a multivariate-Gaussian distribution, i.e. the probability of ϕ respect to fixed ϕ'. In these terms, one can write

$$\begin{cases} \Phi(\phi,\phi') & = g\left[J(\sqrt{C_0 - C^2/C_0}\,\phi + C/\sqrt{C_0}\,\phi') + J_0 M\right] \\ \Psi(\phi) & = g\left[J\sqrt{C_0}\,\phi' + J_0 M\right] \end{cases} \tag{D1}$$

then, by means of the Fubini's theorem, function $\Xi(C, C(0), M)$ becomes

$$\Xi = \int \frac{d\phi}{\sqrt{2\pi}} e^{-\phi^2/2} \tanh(\Psi(\phi)) \left\{ \int \frac{d\phi'}{\sqrt{2\pi}} e^{-\phi'^2/2} \tanh(\Phi(\phi,\phi')) \right\}. \tag{D2}$$

With this simple form, it is straightforward to compute $V(C|C(0), M)$ directly by solving numerically the iterated integrals.

3. Computation of the largest Lyapunov exponent

In order to compute the LLE we use the Bennetin-Wolf algorithm[73,74], that works as follows. Consider a dynamical system described by the vector $\mathbf{x}(t) \in \mathbb{R}^N$ at time $t \geq 0$, which evolves following a differentiable dynamical system given by $\dot{\mathbf{x}}(t) = \mathbf{F}(\mathbf{x}(t))$. In order to integrate it numerically, we construct the map

$$\mathbf{x}_{i+1} = \mathbf{f}(\mathbf{x}_i)$$

where $\mathbf{f}$ is the discretization of the vector function $\mathbf{F}$ (which depends on the integration algorithm used) and $\{\mathbf{x}_i : i = 0, 1, 2, ...\}$ defines the discrete trajectory of the system. We use a simple integration algorithm, i.e. the Euler's method: the vector function is defined as the linear evolution of state $\mathbf{x}$ in a time-step h,

$$\mathbf{f}(\mathbf{x}) \equiv \mathbf{x} + \mathbf{F}(\mathbf{x})\,h.$$

Upon defining the matrix $\mathbf{T}(\mathbf{x}) = \mathcal{J}_{\mathbf{x}}\mathbf{f}$, where $\mathcal{J}_{\mathbf{x}}\mathbf{f}$ is the $N \times N$ Jacobian matrix of the vector function $\mathbf{f}$ at state $\mathbf{x}$, we have $\mathbf{T}(\mathbf{x}_{i+1}) = \mathbf{I} + h\,\mathcal{J}_{\mathbf{x}_{i+1}}\mathbf{F}$. Writing

$$\mathbf{T}^n_{\mathbf{x}_0} = \mathbf{T}(\mathbf{x}_{n-1}) \ldots \mathbf{T}(\mathbf{x}_1)\mathbf{T}(\mathbf{x}_0), \tag{D3}$$

as a matrix product, the LLE can be computed as the limit

$$\Lambda = \lim_{n \longrightarrow \infty} \frac{1}{n} \log \|\mathbf{T}^n_{\mathbf{x}_0}\mathbf{u}\| \tag{D4}$$

for a given vector $\mathbf{u}$, where $\|\mathbf{v}\|$ denotes the norm of the vector $\mathbf{v}$. To implement this method computationally, the Bennetin-Wolf correction[75,76] needs to be used to avoid the divergence of $\mathbf{T}^n_{\mathbf{x}_0}\mathbf{u}$ for large n. The correction consists in normalizing this vector at each step. Hence, fixing a starting point $\mathbf{x}_0$, and defining an initial vector $\mathbf{u}_0 = [1, ..., 1]/\sqrt{N}$, the algorithm is described as follows: for $i = 1, \ldots, T$,

1. Obtain the new state at $i + 1$,

$$\begin{aligned} t_{i+1} = &\; t_i + h \\ \mathbf{x}_{i+1} = &\; \mathbf{x}_i + h\,\mathbf{F}(\mathbf{x}_i) \\ \tilde{\mathbf{u}}_{i+1} = &\; \mathbf{T}(\mathbf{x}_{i+1})\,\mathbf{u}_i \end{aligned}$$

2. Normalize the perturbation vector

$$\mathbf{u}_{i+1} = \tilde{\mathbf{u}}_{i+1}/\|\tilde{\mathbf{u}}_{i+1}\|$$

3. Compute the LLE at time-step $i + 1$,

$$L_{i+1} = L_i + \log(\|\tilde{\mathbf{u}}_{i+1}\|)/t_{i+1}$$

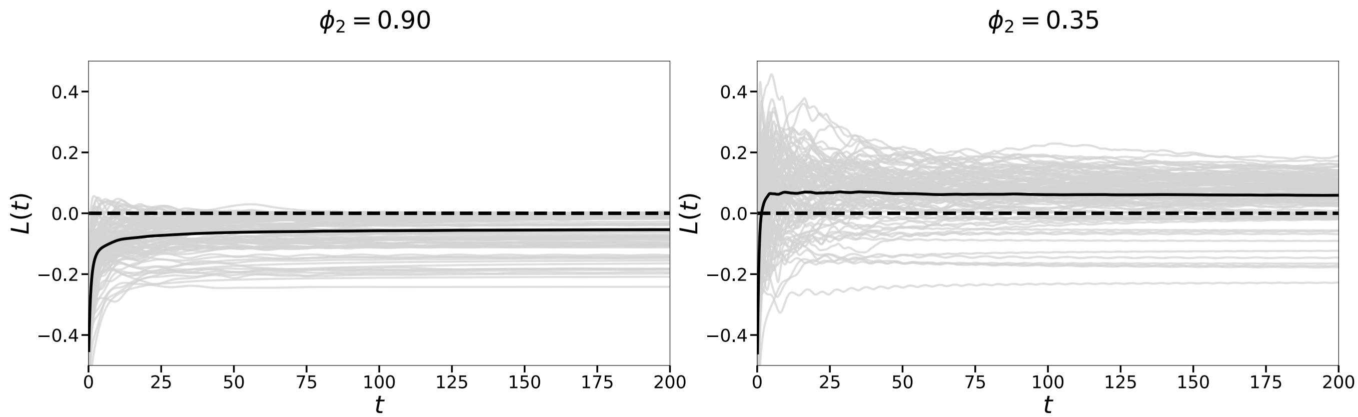

FIG. 13. Computation of largest Lyapunov exponent for $S = 100$ different realizations of a system with $N = 100$, inside the spin-glass regime, above (left panel) and below the onset of chaos (right panel). Each realization is plotted as a grey, solid line, meanwhile the black, solid line is the average over realizations for each time step.

The algorithm gives a set $\{L_i : i = 0, ..., T\}$ of exponents which, in the limit, converge to the LLE of the system, Λ.

Consider now a stochastic differential equation, $\dot{\mathbf{x}}(t) = \mathbf{F}(\mathbf{x}(t)) + \boldsymbol{\xi}(t)$ such that $\boldsymbol{\xi}(t)$ is a (multi-component) white-noise process with zero mean and variance equal to $2\sigma^2$. Hence, the previous algorithm should be modified to introduce the stochastic integration: at step 1., the integration of the trajectory should be replaced by an Euler-Maruyama integration step[72],

$$\mathbf{x}_{i+1} = \mathbf{x}_i + \mathbf{F}(\mathbf{x}_i)h + \sqrt{2h\sigma^2}\mathbf{u}_i \tag{D5}$$

where $\mathbf{u}_i$, for $i = 1, 2, \ldots$, is a set of i.i.d. random Gaussian variables with zero mean and unit variance.

For the dynamical system given by Eq.(1), it is sufficient to fix $h = 0.01$, and integrate the system up to $t_{max} = 200$. As an example, in Fig.13 we show $S = 100$ realizations of the algorithm for a system of size $N = 100$ (grey, solid line) and $\sigma^2 = 0$, each of them initialized with random conditions, $\mathbf{x}_0$ and $\mathbf{J}$. The system is set at $J_0/J = 0.5$ (i.e. inside the spin-glass phase). We show results for $1/gJ = 0.9$ (left panel) and $1/gJ = 0.35$ (right panel). The solid, black line indicates the average over different realizations at each time step, showing that the mean activity is stable (negative LLE) for $1/gJ = 0.9$ and unstable (positive LLE) for $1/gJ = 0.35$. In the latter case, there exists a large amount of unstable trajectories, such that L_i is positive, and some stable trajectories, such that L_i negative, e.g. fixed points.

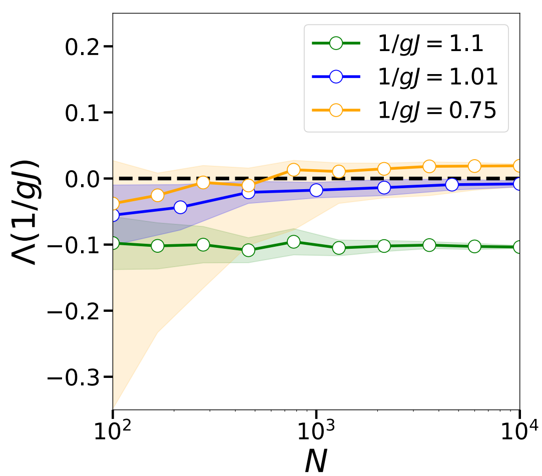

FIG. 14. Averaged largest Lyapunov exponent, Λ, as a function of system size N for a dynamical system with $\sigma^2 = 0$, averaged over $S = 20$ realizations. For $J_0/J = 0.5$, the averaged LLE is computed for three different values of $1/gJ$ (solid lines), as shown in the legend; the standard deviations are shown as shaded areas. Parameter values are as in Fig.13, i.e. $h = 0.01$ and $t_{max} = 200$.

In order to study the convergence, we compute the LLE as a function of the system size N. In Fig.14 we plot, as an example, the LLE Λ, defined as the asymptotic value of $L(t)$ (i.e. the value at $t = 200$), averaged over $S = 20$

realizations, for the particular case of $\sigma = 0$. Fixing $J_0/J = 0.5$, we study three different values of $1/gJ$ in order to characterize the stability of the system in the limit of large system size: $1/gJ = 1.1$ (solid green line) corresponding to the paramagnetic phase; $1/gJ = 1.01$ (solid blue line) falling close to the critical line separating the spin-glass and the paramagnetic region; $1/gJ = 0.75$ (solid orange line), lying in the spin-glass region, away from the critical line. Colored area shows the standard deviation of Λ for each value of N. For $1/gJ > 1$ (blue and green lines), the LLE is typically negative, indicating the existence of stable, fixed point trajectories. In this region, the standard deviation of the LLE is smaller compared to the $1/gJ < 1$ case (orange line). The reason behind this is that, above this critical value of $1/gJ$, the system converges towards fixed point solutions; while below it, finite size effects in the network encourage the appearance of many different trajectories: chaotic, limit cycles and even, occasionally, fixed points, all of it contributing to increasing the standard deviation of the LLE. In practice, for large enough systems (i.e. $N > 1000$) the LLE stabilizes considerably and the standard deviation reduces, as it can be seen in Fig.3.

SUPPLEMENTAL MATERIAL

S.I. GENERATING FUNCTIONAL ANALYSIS

The starting point of the path-integral approach is to divide the time interval of interest $[0, t]$ in $n = t/\Delta$ segments of length Δ, set $t_a = a\Delta \ \forall \ a = 0 \dots n$ and change the differential equation

$$\dot{x}_i = f_i(\mathbf{x}(t)) + \xi_i(t) \tag{S1}$$

with the finite-difference equation

$$x_i^{a+1} - x_i^a = f_i(\mathbf{x}^a)\Delta + \eta_i^a \tag{S2}$$

which is obtained by integrating Eq.(S1) over the time interval $[t_a, t_{a+1}]$, using Euler forward integration. In the above $f_i(\mathbf{x}) = -x_i + \tanh(g\sum_j J_{ij}x_j + \theta_i)$ and we have used the short-hand notation $x_i^a = x_i(t_a)$ and $\eta_i^a = \int_{t_a}^{t_{a+1}} dt\, \xi_i(t)$. Note that η_i^a is a Gaussian white noise with $\langle \eta_i^a \rangle = 0$ and $\langle \eta_i^a \eta_j^b \rangle = 2\sigma^2\Delta\delta_{ab}\,\delta_{ij}$. Next we compute the generating functional

$$Z[\boldsymbol{\psi}] = \left\langle e^{i\sum_{i=1}^N \sum_{a=0}^n x_i^a \psi_i^a} \right\rangle \tag{S3}$$

where the average $\langle \dots \rangle$ is taken over the distribution of the paths $\mathbf{x}^{0\dots n}$

$$p(\mathbf{x}^{0\dots n}) = p(\mathbf{x}^0) \prod_{a=1}^n W(\mathbf{x}^a | \mathbf{x}^{a-1}) \tag{S4}$$

where we have used the Markovianity of dynamics given by Eq.(S2), following from the absence of time correlations in the noise, and denoted with $W(\mathbf{x}^a|\mathbf{x}^{a-1})$ the transition probability from the configuration $\mathbf{x}^{a-1}$ to $\mathbf{x}^a$. Using the conditional independence of the x_i^a's, given the system's configuration $\mathbf{x}^{a-1}$ at the earlier time step, which holds as long as the noise variables at different sites are independent, we can finally write

$$\begin{aligned} p(\mathbf{x}^{0\dots n}) &= p(\mathbf{x}^0) \prod_{a=1}^n \prod_{i=1}^N W(x_i^a | \mathbf{x}^{a-1}) \\ &= p(\mathbf{x}^0) \prod_{a=1}^n \prod_{i=1}^N \int d\eta_i^{a-1} p(\eta_i^{a-1}) \delta(x_i^a - x_i^a(\eta_i^{a-1}, \mathbf{x}^{a-1})) \end{aligned} \tag{S5}$$

where we have denoted $x_i^a(\eta_i^{a-1}, \mathbf{x}^{a-1}) = x_i^{a-1} + f_i(\mathbf{x}^{a-1})\Delta + \eta_i^{a-1}$. This leads to

$$\begin{aligned} Z[\boldsymbol{\psi}] = &\int [\prod_{a=0}^n d\mathbf{x}^a] p_0(\mathbf{x}^0) e^{i\sum_{i=1}^N x_i^0 \psi_i^0} \\ &\times \prod_{a=1}^n \prod_{i=1}^N \int d\eta_i^{a-1} p(\eta_i^{a-1}) \delta(x_i^a - x_i^{a-1} - f_i(\mathbf{x}^{a-1})\Delta - \eta_i^{a-1}) e^{ix_i^a\psi_i^a} \end{aligned} \tag{S6}$$

Using the Fourier representation of the δ-function we then write

$$\begin{aligned} Z[\boldsymbol{\psi}] &= \int \left[\prod_{a=0}^n d\mathbf{x}^a\right] p_0(\mathbf{x}^0) e^{i\sum_{i=1}^N x_i^0\psi_i^0} \int \left[\prod_{a=1}^n \frac{d\hat{\mathbf{x}}^{a-1}}{(2\pi)^N}\right] \\ &\times \prod_{a=1}^n \prod_{i=1}^N \int \frac{d\eta_i^{a-1}}{\sqrt{4\sigma^2\Delta}} e^{-\frac{1}{4\sigma^2\Delta}(\eta_i^{a-1})^2 + i\hat{x}_i^{a-1}[x_i^a - x_i^{a-1} - f_i(\mathbf{x}^{a-1})\Delta - \eta_i^{a-1}] + ix_i^a\psi_i^a} \\ &= \int \left[\prod_{a=0}^n d\mathbf{x}^a\right] p_0(\mathbf{x}^0) e^{i\sum_{i=1}^N x_i^0\psi_i^0} \int \left[\prod_{a=1}^n \frac{d\hat{\mathbf{x}}^{a-1}}{(2\pi)^N}\right] \\ &\times \prod_{a=1}^n \prod_{i=1}^N e^{i\hat{x}_i^{a-1}\Delta[\frac{x_i^a - x_i^{a-1}}{\Delta} - f_i(\mathbf{x}^{a-1})] + ix_i^a\psi_i^a - \sigma^2\Delta(\hat{x}_i^{a-1})^2} \end{aligned} \tag{S7}$$

where we have performed the Gaussian integral. Upon rescaling $\psi_i^a \to \Delta\psi_i^a$, taking the continuous time limit $\Delta \to 0$ and using the definition of Reimann integrals we have

$$Z[\boldsymbol{\psi}] = \int \mathcal{D}\mathbf{x}\mathcal{D}\hat{\mathbf{x}}\, p_0(\mathbf{x}^0) e^{\sum_i \int dt \{i\hat{x}_i(t)[\dot{x}_i(t) - f_i(\mathbf{x}(t))] + ix_i(t)\psi_i(t) - \sigma^2 \hat{x}_i^2(t)\}} \tag{S8}$$

where

$$\mathcal{D}\mathbf{x} = \lim_{\Delta\to 0} \prod_{a=0}^{t/\Delta} d\mathbf{x}^a \quad \text{and} \quad \mathcal{D}\hat{\mathbf{x}} = \lim_{\Delta\to 0} \prod_{a=0}^{t/\Delta} \frac{d\hat{\mathbf{x}}^a}{(2\pi)^N} \tag{S9}$$

In order to carry out the average over the disorder $P(\mathbf{J})$, it is convenient to introduce

$$1 = \lim_{\Delta\to 0} \int \prod_{i=1}^{N} \prod_{a=0}^{t/\Delta} dz_i^a\, \delta(z_i^a - g\sum_j J_{ij} x_j^a - \theta_i) = \int \mathcal{D}\mathbf{z}\mathcal{D}\hat{\mathbf{z}} e^{i\sum_i \int dt\, \hat{z}_i(t)[z_i(t) - g\sum_j J_{ij} x_j(t) - \theta_i(t)]} \tag{S10}$$

leading to

$$\begin{aligned}\overline{Z[\boldsymbol{\psi}]} = &\int \mathcal{D}\mathbf{x}\mathcal{D}\hat{\mathbf{x}}\, p_0(\mathbf{x}^0) \int \mathcal{D}\mathbf{z}\mathcal{D}\hat{\mathbf{z}} e^{\sum_i \int dt \{i\hat{x}_i(t)[\dot{x}_i(t) + x_i - \tanh(z_i)] + ix_i(t)\psi_i(t) - \sigma^2 \hat{x}_i^2(t)\}} \\ &\times e^{\sum_i \int dt \{i\hat{z}_i(t)[z_i(t) - \theta_i(t)]\}}\, \overline{e^{-ig\int dt\, \sum_{ij} J_{ij}\hat{z}_i(t) x_j(t)}}\end{aligned} \tag{S11}$$

The last term of Eq.(S11) can be worked out as follows

$$\begin{aligned}&\overline{e^{-i\int dt\, g\sum_{ij} J_{ij}\hat{z}_i(t)x_j(t)}} = \overline{e^{-i\int dt\, g\sum_{i<j}[J_{ij}\hat{z}_i(t)x_j(t) + J_{ji}\hat{z}_j(t)x_i(t)] - i\int dt\, g\sum_i J_{ii}\hat{z}_i(t)x_i(t)}} \\ &= \left[\prod_{i<j} \int dJ_{ij} dJ_{ji} P(J_{ji}, J_{ij}) e^{-i\int dt\, g[J_{ij}\hat{z}_i(t)x_j(t) + J_{ji}\hat{z}_j(t)x_i(t)]}\right] \left[\prod_i \int dJ_{ii} P(J_{ii}) e^{-igJ_{ii}\int dt\, \hat{z}_i(t)x_i(t)}\right] \\ &= \left[\prod_{i<j} \int \frac{d\mathbf{u}}{2\pi\sqrt{\det \boldsymbol{\Sigma}}} e^{-\frac{1}{2}(\mathbf{u}-\boldsymbol{\mu})^T \boldsymbol{\Sigma}^{-1}(\mathbf{u}-\boldsymbol{\mu})} e^{-i\mathbf{b}_{ij}^T \mathbf{u}}\right] \left[\prod_i \int \frac{dJ_{ii}}{\sqrt{2\pi}} e^{-\frac{N}{2J^2}\left(J_{ii} - \frac{J_0}{N}\right)^2} e^{-igJ_{ii}\int dt\, \hat{z}_i(t)x_i(t)}\right]\end{aligned} \tag{S12}$$

where $\mathbf{u}^T = (J_{ij}, J_{ji})$, with T denoting the transpose,

$$\boldsymbol{\mu} = \begin{pmatrix} J_0/N \\ J_0/N \end{pmatrix} \qquad \boldsymbol{\Sigma} = \frac{J^2}{N}\begin{pmatrix} 1 & \gamma \\ \gamma & 1 \end{pmatrix} \tag{S13}$$

and $\mathbf{b}_{ij}^T = (A_{ij}, B_{ji})$ with $A_{ij} = g\int dt\, \hat{z}_i(t)x_j(t)$ and $B_{ji} = g\int dt\, \hat{z}_j(t)x_i(t)]$. Shifting the integration variables and executing the Gaussian integral, the expressions above become, respectively

$$\overline{e^{-i\int dt\, g\sum_i J_{ii}\hat{z}_i(t)x_i(t)}} = \left[\prod_i e^{-ig\frac{J_0}{N}\int dt\, \hat{z}_i(t)x_i(t) - \frac{g^2 J^2}{2N}\int dt\, dt', \hat{z}_i(t)x_i(t)\hat{z}_i(t')x_i(t')}\right] \tag{S14}$$

and

$$\begin{aligned}&\overline{e^{-i\int dt\, g\sum_{i<j}[J_{ij}\hat{z}_i(t)x_j(t) + J_{ji}\hat{z}_j(t)x_i(t)]}} = e^{-i\sum_{i<j}\mathbf{b}_{ij}^T\boldsymbol{\mu}} \prod_{i<j} \int \frac{d\mathbf{v}}{2\pi\sqrt{\det\boldsymbol{\Sigma}}} e^{-\frac{1}{2}\mathbf{v}^T\boldsymbol{\Sigma}^{-1}\mathbf{v}} e^{-i\mathbf{b}_{ij}^T\mathbf{v}} \\ &= e^{-i\sum_{i<j}\mathbf{b}_{ij}^T\boldsymbol{\mu}} \prod_{i<j} e^{-\frac{1}{2}\mathbf{b}_{ij}^T\boldsymbol{\Sigma}\mathbf{b}_{ij}} = e^{-i\sum_{i<j}\frac{J_0}{N}(A_{ij}+B_{ji})} e^{-\frac{J^2}{2N}\sum_{i<j}(A_{ij}^2 + \gamma A_{ij}B_{ji} + \gamma B_{ji}A_{ij} + B_{ji}^2)} \\ &= e^{-ig\frac{J_0}{N}\int dt\, \sum_{i<j}[\hat{z}_i(t)x_j(t) + \hat{z}_j(t)x_i(t)] - \frac{g^2 J^2}{2N}\int dt\, dt'\, \sum_{i<j}[\hat{z}_i(t)x_j(t)\hat{z}_i(t')x_j(t') + \hat{z}_j(t)x_i(t)\hat{z}_j(t')x_i(t')]} \\ &\quad\times e^{-\gamma\frac{g^2 J^2}{2N}\int dt\, dt'\, \sum_{i<j}[\hat{z}_i(t)x_j(t)\hat{z}_j(t')x_i(t') + \hat{z}_j(t)x_i(t)\hat{z}_i(t')x_j(t')]}\end{aligned} \tag{S15}$$

Upon introducing the following order functions:

$$M(t) = \frac{1}{N}\sum_i x_i(t) \tag{S16}$$

$$Q(t) = \frac{1}{N}\sum_i \hat{z}_i(t) \tag{S17}$$

$$C(t,t') = \frac{1}{N}\sum_i x_i(t)x_i(t') \tag{S18}$$

$$L(t,t') = \frac{1}{N}\sum_i \hat{z}_i(t)\hat{z}_i(t') \tag{S19}$$

$$K(t,t') = \frac{1}{N}\sum_i x_i(t)\hat{z}_i(t') \tag{S20}$$

$$J(t,t') = \frac{1}{N}\sum_i x_i(t)\hat{z}_i(t)x_i(t')\hat{z}_i(t') \tag{S21}$$

via suitable delta-functions, using their Fourier representations, and assuming a factorised initial distribution $p_0(\mathbf{x}^0) = \prod_i p_{i0}(x_i^0)$, the disorder-averaged generating functional

$$\overline{Z[\boldsymbol{\psi}]} = \int \mathcal{D}M \,\ldots\, \mathcal{D}\hat{L}\, e^{N[\Psi+\Phi+\Omega]} \tag{S22}$$

of a dynamical field theory for the fields $M, Q, C, L, \hat{M}, \hat{Q}, \hat{C}, \hat{L}$ described by the action $S = \Psi + \Phi + \Omega$, where

$$\begin{aligned}
\Psi &= i\int dt\,[M(t)\hat{M}(t) + Q(t)\hat{Q}(t)] + i\int dt\,dt'\,[C(t,t')\hat{C}(t,t') + L(t,t')\hat{L}(t,t') + K(t,t')\hat{K}(t,t') + J(t,t')\hat{J}(t,t')] \\
\Phi &= -iJ_0 g\int dt\left[Q(t)M(t) + \frac{1}{N}K(t,t)\right] - \frac{J^2g^2}{2}\int dt'\left[L(t,t')C(t,t') + \gamma K(t,t')K(t',t) + \frac{1}{N}J(t,t')\right] \\
\Omega &= \frac{1}{N}\sum_i \log\int \mathcal{D}x_i\mathcal{D}\hat{x}_i\mathcal{D}z_i\mathcal{D}\hat{z}_i\, p_{i0}(x_i^0) \\
&\quad\times e^{\int dt\{i\hat{x}_i(t)[\dot{x}_i(t)+x_i-\tanh(z_i)]+ix_i(t)\psi_i(t)-\sigma^2\hat{x}_i^2(t)+i\hat{z}_i(t)[z_i(t)-\theta_i(t)]\}} \\
&\quad\times e^{-i\int dt\,[\hat{M}(t)x_i(t)+\hat{Q}(t)\hat{z}_i(t)]} \\
&\quad\times e^{-i\int dt\,dt'\,[\hat{C}(t,t')x_i(t)x_i(t')+\hat{L}(t,t')\hat{z}_i(t)\hat{z}_i(t')+\hat{K}(t,t')x_i(t)\hat{z}_i(t')+\hat{J}(t,t')x_i(t)\hat{z}_i(t)x_i(t')\hat{z}_i(t')]}
\end{aligned} \tag{S23}$$

In the limit $N \to \infty$ we can calculate the integral in Eq.(S22) by steepest-descent. Maximizing the exponent in the integral $S = \Psi + \Phi + \Omega$ with respect to the dynamical order parameters and their conjugate variables, we get

$$\begin{aligned}
\frac{\delta S}{\delta M(t)} = 0 \quad&\Rightarrow\quad i\hat{M}(t) = iJ_0 g Q(t) \\
\frac{\delta S}{\delta Q(t)} = 0 \quad&\Rightarrow\quad i\hat{Q}(t) = iJ_0 g M(t) \\
\frac{\delta S}{\delta C(t,t')} = 0 \quad&\Rightarrow\quad i\hat{C}(t,t') = \frac{J^2g^2}{2}L(t,t') \\
\frac{\delta S}{\delta L(t,t')} = 0 \quad&\Rightarrow\quad i\hat{L}(t,t') = \frac{J^2g^2}{2}C(t,t') \\
\frac{\delta S}{\delta K(t,t')} = 0 \quad&\Rightarrow\quad i\hat{K}(t,t') = \gamma J^2g^2K(t',t) \\
\frac{\delta S}{\delta J(t,t')} = 0 \quad&\Rightarrow\quad i\hat{J}(t,t') = 0
\end{aligned} \tag{S24}$$

and

$$\frac{\delta S}{\delta \hat{M}(t)} = 0 \quad \Rightarrow \quad M(t) = \lim_{N\to\infty} \frac{1}{N} \sum_i \langle x(t) \rangle_{\omega_i}$$
$$\frac{\delta S}{\delta \hat{Q}(t)} = 0 \quad \Rightarrow \quad Q(t) = \lim_{N\to\infty} \frac{1}{N} \sum_i \langle \hat{z}(t) \rangle_{\omega_i}$$
$$\frac{\delta S}{\delta \hat{C}(t,t')} = 0 \quad \Rightarrow \quad C(t,t') = \lim_{N\to\infty} \frac{1}{N} \sum_i \langle x(t)\hat{x}(t') \rangle_{\omega_i}$$
$$\frac{\delta S}{\delta \hat{L}(t,t')} = 0 \quad \Rightarrow \quad L(t,t') = \lim_{N\to\infty} \frac{1}{N} \sum_i \langle \hat{z}(t)\hat{z}(t') \rangle_{\omega_i}$$
$$\frac{\delta S}{\delta \hat{K}(t,t')} = 0 \quad \Rightarrow \quad K(t,t') = \lim_{N\to\infty} \frac{1}{N} \sum_i \langle x(t)\hat{z}(t') \rangle_{\omega_i}$$
$$\frac{\delta S}{\delta \hat{J}(t,t')} = 0 \quad \Rightarrow \quad J(t,t') = \lim_{N\to\infty} \frac{1}{N} \sum_i \langle x(t)\hat{z}(t)x(t')\hat{z}(t') \rangle_{\omega_i} \tag{S25}$$

where we have introduced the notation

$$\langle \,\cdot\, \rangle_{\omega_i} = \frac{\int \mathcal{D}x\mathcal{D}\hat{x}\mathcal{D}z\mathcal{D}\hat{z} p_{i0}(x^0) \,\cdot\, e^{s_i}}{\int \mathcal{D}x\mathcal{D}\hat{x}\mathcal{D}z\mathcal{D}\hat{z} p_{i0}(x^0)\, e^{s_i}} \tag{S26}$$

with s_i denoting the effective single-particle action

$$\begin{aligned} s_i = \int dt \{ & i\hat{x}(t)[\dot{x}(t) + x - \tanh(z)] + ix(t)\psi_i(t) - T\hat{x}^2(t) + i\hat{z}(t)[z(t) - \theta_i(t)] \\ & - i[\hat{M}(t)x(t) + \hat{Q}(t)\hat{z}(t)]\} - i \int dt\, dt' \, [\hat{C}(t,t')x(t)x(t') + \hat{L}(t,t')\hat{z}(t)\hat{z}(t') \\ & + \hat{K}(t,t')x(t)\hat{z}(t') + \hat{J}(t,t')x(t)\hat{z}(t)x(t')\hat{z}(t')] \end{aligned} \tag{S27}$$

Next, we assume $\theta_i(t) = \theta(t)$ and $p_{i0}(x^0) = p_0(x^0)$ for all i. In this case, s_i (and thus $\langle \cdot \rangle_{\omega_i}$) depends on i only through ψ_i, which is however set to zero when computing the dynamical observables we are interested in (see Eqs.(7), (8) and (9)). Thus, from Eq.(7), differentiating $\bar{Z}[\boldsymbol{\psi}]$ w.r.t. $\psi_i(t)$, setting $\boldsymbol{\psi} = \mathbf{0}$ and taking the limit $N \to \infty$, we obtain

$$\begin{aligned} \overline{\langle x_i(t) \rangle} &= \frac{\delta \overline{Z[\boldsymbol{\psi}]}}{i\delta\psi_i(t)}\Big|_{\boldsymbol{\psi}=\mathbf{0}} \\ &= \lim_{N\to\infty} \int \mathcal{D}M \,\ldots\, \mathcal{D}\hat{N}\, e^{N[\Psi+\Phi+\Omega]} \langle x(t) \rangle_{\omega_i} \Big|_{\boldsymbol{\psi}=\mathbf{0}} \\ &= \lim_{N\to\infty} \frac{\int \mathcal{D}M \,\ldots\, \mathcal{D}\hat{N}\, e^{N[\Psi+\Phi+\Omega]} \langle x(t) \rangle_{\omega_i}}{\int \mathcal{D}M \,\ldots\, \mathcal{D}\hat{N}\, e^{N[\Psi+\Phi+\Omega]}} \Big|_{\boldsymbol{\psi}=\mathbf{0}} = \langle x(t) \rangle_{\omega} \end{aligned} \tag{S28}$$

where we have used Eq.(S22) and $Z[\mathbf{0}] = 1$ and used the notation

$$\langle \,\cdot\, \rangle_{\omega} = \frac{\int \mathcal{D}x\mathcal{D}\hat{x}\mathcal{D}z\mathcal{D}\hat{z} p_0(x^0) \,\cdot\, e^{s}}{\int \mathcal{D}x\mathcal{D}\hat{x}\mathcal{D}z\mathcal{D}\hat{z} p_0(x^0)\, e^{s}} \tag{S29}$$

and

$$\begin{aligned} s = \int dt \{ & i\hat{x}(t)[\dot{x}(t) + x - \tanh(z)] - \sigma^2\hat{x}^2(t) + i\hat{z}(t)[z(t) - \theta(t)] - i[\hat{M}(t)x(t) + \hat{Q}(t)\hat{z}(t)]\} \\ & - i \int dt\, dt' \, [\hat{C}(t,t')x(t)x(t') + \hat{L}(t,t')\hat{z}(t)\hat{z}(t') + \hat{K}(t,t')x(t)\hat{z}(t') + \hat{J}(t,t')x(t)\hat{z}(t)x(t')\hat{z}(t')] \end{aligned} \tag{S30}$$

with

$$\begin{aligned} M(t) &= \langle x(t) \rangle_{\omega} \\ Q(t) &= \langle \hat{z}(t) \rangle_{\omega} \\ C(t,t') &= \langle x(t)x(t') \rangle_{\omega} \\ L(t,t') &= \langle \hat{z}(t)\hat{z}(t') \rangle_{\omega} \\ K(t,t') &= \langle x(t)\hat{z}(t') \rangle_{\omega} \\ J(t,t') &= \langle x(t)\hat{z}(t)x(t')\hat{z}(t') \rangle_{\omega} \end{aligned} \tag{S31}$$

Similarly, using Eqs.(8) and (9), we obtain

$$C_{ij}(t,t') = \overline{\langle x_i(t)x_j(t')\rangle} = \frac{\delta^2 \overline{Z[\boldsymbol{\psi}]}}{i\delta\psi_i(t)i\delta\psi_j(t')}|_{\boldsymbol{\psi}=\mathbf{0}} = \langle x(t)x(t')\rangle_\omega \equiv C(t,t') \tag{S32}$$

and

$$R_{ij}(t,t') = \frac{\overline{\delta\langle x_i(t)\rangle}}{\delta\theta_j(t')} = \frac{\delta}{\delta\theta_j(t')}\left[\frac{\delta\overline{Z[\boldsymbol{\psi}]}}{i\delta\psi_i(t)}|_{\boldsymbol{\psi}=\mathbf{0}}\right] = -i\langle x(t)\hat{z}(t')\rangle_\omega \equiv R(t,t') \tag{S33}$$

having defined $R(t,t') = -iK(t,t')$. Additional relations follow from $Z[\mathbf{0}] = 1$, implying that moments involving only $\hat{z}$-fields vanish, e.g.

$$\frac{\delta}{\delta i\theta(t)}\overline{Z[\mathbf{0}]} = -\langle\hat{z}(t)\rangle_\omega = 0, \qquad \frac{\delta^2}{\delta i\theta(t)\delta i\theta(t')}\overline{Z[\mathbf{0}]} = \langle\hat{z}(t)z(t')\rangle_\omega = 0 \tag{S34}$$

Hence,

$$Q(t) = 0 \quad \Rightarrow \quad \hat{M}(t) = 0 \tag{S35}$$

$$L(t,t') = 0 \quad \Rightarrow \quad \hat{C}(t,t') = 0 \tag{S36}$$

Finally, we substitute previous equations and Eq.(S24) into Eq.(S30) and we write Eq.(S29) as

$$\langle\,\cdot\,\rangle_\omega = \frac{\int\mathcal{D}x\,\cdot\,P[x]}{\int\mathcal{D}x\,P[x]} \tag{S37}$$

thus obtaining

$$\begin{aligned} P[x] &= p_0(x^0)\int\mathcal{D}\hat{x}\mathcal{D}z\mathcal{D}\hat{z}e^s \\ &= p_0(x^0)\int\mathcal{D}\hat{x}\mathcal{D}z\mathcal{D}\hat{z}\,e^{\int dt\{i\hat{x}(t)[\dot{x}(t)+x-\tanh(z)]-\sigma^2\hat{x}^2(t)\}} \\ &\quad\times e^{-\frac{J^2g^2}{2}\int dt\,dt'\,C(t,t')\hat{z}(t)\hat{z}(t')}e^{i\int dt\,[z(t)-J_0gM(t)-\gamma g^2J^2\int dt'\,R(t,t')x(t')-\theta(t)]\hat{z}(t)} \end{aligned} \tag{S38}$$

Applying Gaussian linearization to the quadratic terms in the exponential and performing the path integrals over $\hat{x}(t)$, $\hat{z}(t)$ and $z(t)$, we get

$$\begin{aligned} P[x] &= p_0(x^0)\int\mathcal{D}\hat{x}\mathcal{D}z\mathcal{D}\hat{z}\mathcal{D}\xi\mathcal{D}\phi\,e^{-\frac{1}{4\sigma^2}\int dt\,\xi^2(t)+\int dt\{i\hat{x}(t)[\dot{x}(t)+x-\tanh(z)-\xi(t)]\}} \\ &\quad\times e^{-\frac{1}{2J^2g^2}\int dt\,dt'\,\phi(t)C^{-1}(t,t')\phi(t')}e^{i\int dt\,[z(t)-J_0gM(t)-\gamma g^2J^2\int dt'\,R(t,t')x(t')-\theta(t)-\phi(t)]\hat{z}(t)\}} \\ &= p_0(x^0)\int\mathcal{D}z\mathcal{D}\xi\mathcal{D}\phi\,e^{-\frac{1}{4\sigma^2}\int dt\,\xi^2(t)}\prod_t\delta[\dot{x}(t)+x-\tanh(z)-\xi(t)] \\ &\quad\times e^{-\frac{1}{2J^2g^2}\int dt\,dt'\,\phi(t)C^{-1}(t,t')\phi(t')}\prod_t\delta[z(t)-J_0gM(t)-\gamma g^2J^2\int dt'\,R(t,t')x(t')-\theta(t)-\phi(t)] \\ &= p_0(x^0)\int\mathcal{D}\xi\mathcal{D}\phi\,e^{-\frac{1}{4\sigma^2}\int dt\,\xi^2(t)}e^{-\frac{1}{2J^2g^2}\int dt\,dt'\,\phi(t)C^{-1}(t,t')\phi(t')} \\ &\quad\times\prod_t\delta\left\{\dot{x}(t)+x-\tanh\left[J_0gM(t)+\gamma g^2J^2\int dt'\,R(t,t')x(t')+\theta(t)+\phi(t)\right]-\xi(t)\right\} \end{aligned} \tag{S39}$$

This is the probability of observing a path $x(t)$ of the effective process described by equation Eq.(10).

S.II. ALTERNATIVE DERIVATION OF FIXED POINT EQUATIONS FOR $\sigma = \gamma = 0$

In this section we provide a simpler derivation of the equations for the fixed points of the noiseless dynamics (which does not require the path integral approach described in the earlier section). Such derivation is however only valid for the case of uncorrelated interactions ($\gamma = 0$). Assuming the scenario where the system reaches a stable fixed point solution $(x_1, \ldots, x_N)$, one has

$$x_i = \tanh\left(g \sum_j J_{ij} x_j\right). \tag{S40}$$

Introducing the order parameter

$$q^{(n)} = \frac{1}{N} \sum_i x_i^n \tag{S41}$$

we can write

$$\begin{aligned} q^{(n)} &= \frac{1}{N} \sum_i \tanh^n \Big(g \sum_j J_{ij} x_j\Big) \\ &= \frac{1}{N} \sum_i \int dJ_1 \ldots dJ_N \delta(J_1 - J_{i1}) \ldots \delta(J_N - J_{iN}) \tanh^n \Big(g \sum_j J_j x_j\Big) \\ &= \int d\mathbf{J} P(\mathbf{J}) \tanh^n \Big(g \sum_j J_j x_j\Big) \end{aligned} \tag{S42}$$

where we have defined

$$P(\mathbf{J}) = P(J_1, \ldots, J_N) = \frac{1}{N} \sum_i \prod_\ell \delta(J_\ell - j_{i\ell})$$

as the distribution of the interactions to a randomly picked node i. Introducing

$$1 = \int dz\, \delta(z - \sum_j J_j x_j)$$

in Fourier representation, we can write

$$\begin{aligned} q^{(n)} &= \int dz \tanh^n(gz) \int \frac{d\hat{z}}{2\pi} e^{i\hat{z}z} \int d\mathbf{J} P(\mathbf{J}) e^{-i\hat{z}\sum_j J_j x_j} \\ &= \int dz \tanh^n(gz) \int \frac{d\hat{z}}{2\pi} e^{i\hat{z}z} e^{\sum_j \log \int dJ P(J) e^{-i\hat{z}J x_j}} \end{aligned} \tag{S43}$$

where we have used the independence of the J_j's, i.e. $P(\mathbf{J}) = \prod_j P(J_j)$. If each J_j is drawn from a Gaussian distribution, $P(J) = \mathcal{N}(J_0/N, J^2/N)$, one obtains

$$\int dJ P(J) e^{-i\hat{z}J x_j} = e^{-\frac{J^2 \hat{z}^2 x_j^2}{2N} - i\frac{\hat{z} J_0 x_j}{N}}$$

and

$$\begin{aligned} q^{(n)} &= \int dz \tanh^n(gz) \int \frac{d\hat{z}}{2\pi} e^{i\hat{z}z - \frac{J^2 \hat{z}^2 q^{(2)}}{2} - i\hat{z} J_0 q^{(1)}} \\ &= \int \frac{dz}{\sqrt{2\pi q^{(2)} J^2}} \tanh^n(gz) \int \frac{d\hat{z}}{\sqrt{2\pi / q^{(2)} t J^2}} e^{i\hat{z}(z - J_0 q^{(1)}) - \frac{J^2 \hat{z}^2 q^{(2)}}{2}} \\ &= \int \frac{dz}{\sqrt{2\pi q^{(2)} J^2}} e^{-\frac{(z - J_0 q^{(1)})^2}{2J^2 q^{(2)}}} \tanh^n(gz) \\ &= \int \frac{dz}{\sqrt{2\pi}} e^{-\frac{z^2}{2}} \tanh^n \Big[g\Big(zJ\sqrt{q^{(2)}} + J_0 q^{(1)}\Big)\Big] \end{aligned} \tag{S44}$$

This leads to a closed set of equations for $n = 1, 2$, which, by denoting $M = q^{(1)}$ and $q = q^{(2)}$, read as (16) and (17).

S.III. PHASE DIAGRAM AND CRITICAL EXPONENTS OF FIXED-POINT SOLUTIONS FOR $\sigma = 0$ AND $\gamma = 0$

For $g = 0$, the solution of the set of Eqs.(16)-(17) is $(M, q) = (0, 0)$. This solution exists for all values of g, however it is expected to become unstable at higher values of g, where a non-trivial solution emerges. Bifurcations of non-trivial solutions from $(0, 0)$ can be found by expanding to linear order in M and $q = 0$

$$\begin{aligned} M &= \int \frac{dz}{\sqrt{2\pi}} e^{-\frac{z^2}{2}} \Big(gJ_0 M\Big) = gJ_0 M \\ q &= \int \frac{dz}{\sqrt{2\pi}} e^{-\frac{z^2}{2}} \Big[\Big(gzJ\sqrt{q}\Big)^2 + (gJ_0 M)^2\Big] = g^2 J^2 q + g^2 J_0^2 M^2 \end{aligned} \tag{S45}$$

Bifurcations from $M = 0$ to $M \neq 0$ will occur at $gJ_0 \geq 1$. For $gJ_0 < 1$, $M = 0$ and bifurcations from $(0, 0)$ to $(0, q)$ will occur at $gJ \geq 1$, provided that $J_0 < J$. Conversely, for $J_0 > J$, bifurcations will occur at $gJ_0 \geq 1$ from $(0, 0)$ to (M, q). Hence, bifurcations from $(0, 0)$ will occur at $g = \min(J^{-1}, J_0^{-1})$ or $1/g = \max(J, J_0)$, which gives the result Eq.(4). Next, we derive the asymptotic behaviour of M and q close to criticality, for the case $J_0 > J$ and $J_0 < J$.

For $J_0 > J$, where both M and q become non-zero at $g = J_0^{-1}$, one expands Eq.(16) and Eq.(17), for small M and q, to the first sub-leading order, at $gJ_0 = 1 + \epsilon$. The equation for M gives

$$\begin{aligned} M &\simeq \int \frac{dz}{\sqrt{2\pi}} e^{-\frac{z^2}{2}} \Big\{\Big(gJ_0 M\Big) - \frac{1}{3}\Big[\Big(gJ_0 M\Big)^3 + 3g^3 J_0 M J^2 q\Big]\Big\} \\ &= (1 + \epsilon)M - \frac{1}{3}(1 + \epsilon)^3 M^3 - \frac{J^2}{J_0^2}(1 + \epsilon)^3 M q \end{aligned} \tag{S46}$$

The non-zero solution is given, to $\mathcal{O}(\epsilon)$, by

$$M^2 \simeq 3\epsilon - 3\frac{J^2}{J_0^2} q \tag{S47}$$

Anticipating that $q \simeq g^2 J_0^2 M^2/(1 - g^2 J^2)$ (see Eq.(S49)) and using $\epsilon = gJ_0 - 1$, we get

$$M = (gJ_0 - 1)^{1/2} \sqrt{3\frac{J_0^2 - J^2}{J_0^2 + 2J^2}} \tag{S48}$$

Expanding the equation for q we have $q \simeq g^2 J_0^2 M^2 + g^2 J^2 q$, hence, rearranging and substituting Eq.(S48) we find

$$q = \frac{g^2 J_0^2 M^2}{1 - g^2 J^2} = 3\frac{J_0^2}{J_0^2 + 2J^2}(gJ_0 - 1) \tag{S49}$$

On the other hand, for $J_0 < J$, q will bifurcate first and its asymptotic behaviour at $gJ = 1 + \epsilon$ is found by expanding Eq.(17) for small q to the first sub-leading order (and setting $M = 0$)

$$\begin{aligned} q &\simeq \int \frac{dz}{\sqrt{2\pi}} e^{-\frac{z^2}{2}} \Big[\Big(gzJ\sqrt{q}\Big) - \frac{1}{3}\Big(gzJ\sqrt{q}\Big)^3\Big]^2 \simeq \int \frac{dz}{\sqrt{2\pi}} e^{-\frac{z^2}{2}} \Big[\Big(gzJ\sqrt{q}\Big)^2 - \frac{2}{3}\Big(gzJ\sqrt{q}\Big)^4\Big] \\ &= g^2 J^2 q - \frac{2}{3} g^4 J^4 q^2 \cdot 3 = (1 + \epsilon)^2 q - 2(1 + \epsilon)^4 q^2 = (1 + 2\epsilon)q - 2(1 + 4\epsilon)q^2 \end{aligned} \tag{S50}$$

where we have used that $\langle z^4 \rangle = 3\langle \sigma^2 \rangle^2$ for a zero-averaged Gaussian variable z with variance σ^2. This gives $\epsilon = (1 + 4\epsilon)q \simeq q$ hence

$$q \simeq (gJ - 1) \tag{S51}$$

Summarizing, close to the transition line the asymptotic behavior of M and q follows a power law as given in Eqs. (S48) and (S49), for $J > J_0$ and (S51), for $J_0 < J$. These can be simplified to

$$M \sim (g - g_c)^{\alpha} \qquad \text{and} \qquad q \sim (g - g_c)^{\beta}$$

where the exponents α and β and the critical point g_c are given in Tab.S1. The asymptotic behaviour of M and q close to the critical point is shown by the full solid lines in panels (C) and (D) of Fig.2, respectively.

	α	β	g_c
$J_0 < J$	–	1	1/J
$J_0 > J$	1/2	1	$1/J_0$

TABLE S1. Critical exponents α and β for M and q, respectively, close to the bifurcation point g_c. These values change depending on the values of J_0 and J.

Finally, the critical line at which bifurcations from $(0, q)$ to (M, q) occur can be found expanding Eq.(16) for small M at $q \neq 0$

$$\begin{aligned} M &\simeq \int \frac{dz}{\sqrt{2\pi}} e^{-\frac{z^2}{2}} \Big\{ \tanh\left(gzJ\sqrt{q}\right) + gJ_0M\Big[1 - \tanh^2\left(gzJ\sqrt{q}\right)\Big]\Big\} \\ &= gJ_0M\Big[1 - \int \frac{dz}{\sqrt{2\pi}} e^{-\frac{z^2}{2}} \tanh^2\left(gzJ\sqrt{q}\right)\Big] = gJ_0M(1-q) \end{aligned} \tag{S52}$$

which leads to Eq.(18) where q is the solution of Eq.(19).

S.IV. REACTIVITY BIFURCATION ANALYSIS

This section is dedicated to complementing and extending the previous linear stability analysis, which primarily focuses on the long-term response to small perturbations. Instead, now we focus into transient dynamics, which can play a significant role as perturbations may be strongly amplified before the system relaxes to its steady state. For instance, in the context of ecological systems, the amplification of a small perturbation can drive the system far from the steady state, increasing the risk of stochastic extinction[45]. Different types of measures have been proposed to study transient dynamics. Here, we focus on *reactivity*[44,45,77] as it measures the maximal amplification rate of a perturbation.

Consider a system evolving by a dynamical equation $\dot{\mathbf{x}}(t) = \mathbf{F}(\mathbf{x}(t))$, and assume that $\mathbf{x}^*$ is a steady-state of the system, i.e. $\mathbf{F}(\mathbf{x}^*) = 0$. The response of the system against small perturbations $\mathbf{y}$ of the steady state, i.e. $\mathbf{x} = \mathbf{x}^* + \mathbf{y}$, is well-described by the linearized dynamics $\dot{\mathbf{y}}(t) = \mathcal{J}_{\mathbf{x}^*}\mathbf{F}\,\mathbf{y}(t)$, where $\mathcal{J}_{\mathbf{x}^*}\mathbf{F}$ is the Jacobian matrix of $\mathbf{F}$ at the steady state. We define the *reactivity* parameter as

$$R = \max_{\mathbf{y_0}} \left(\frac{d}{dt} \log \|\mathbf{y}(t)\| \Big|_{t=0} \right) \tag{S53}$$

where the maximum is taken over all initial conditions $\mathbf{y}(0) = \mathbf{y}_0$. Note that, as the evolution of the linear perturbation follows an exponential form $\mathbf{y}(t) \sim e^{\alpha(t)t}$, the reactivity parameter coincides with the initial exponential ratio $R = \alpha(0)$. Hence, the perturbation vanishes quickly if $R < 0$, and the system is called non-reactive; while the perturbation is initially amplified if $R > 0$, and the system is said to be reactive. Furthermore, it can be easily proved that the reactivity R is equivalent to the largest eigenvalue of $\mathbf{H} = \frac{1}{2}(\mathcal{J}_{\mathbf{x}^*}\mathbf{F} + \mathcal{J}_{\mathbf{x}^*}\mathbf{F}^T)$, the symmetric part of the Jacobian matrix[44,45,49].

For our system Eq.(1), and assuming noiseless dynamics ($\sigma = 0$) and $\theta = 0$, the steady-state is trivially $\mathbf{x} = 0$ in the paramagnetic regime. The Jacobian matrix is given by $g\,\mathbf{J} - \mathbf{I}$, where $\mathbf{J}$ is a Gaussian matrix defined by parameters (J_0, J, γ), described in Eqs. (2 - 3). Hence, the symmetric part is given by the expression

$$\mathbf{H} = \frac{g}{2}\,(\mathbf{J} + \mathbf{J}^T) - \mathbf{I} = g\mathbf{A} - \mathbf{I}$$

where matrix $\mathbf{A}$ is nothing but a symmetric Gaussian matrix with mean and variance given by

$$\overline{A_{ij}} = \frac{J_0}{N} \quad \text{and} \quad \overline{A_{ij}^2} - \frac{J_0^2}{N^2} = \frac{1}{2}(1+\gamma)\frac{J^2}{N} \tag{S54}$$

The reactivity bifurcation, defined as the point in the parameter space at which the system becomes reactive, can be computed by simply analysing the distribution of eigenvalues of matrix $\mathbf{A}$. In the same terms as in Sec.III, the bifurcation lines are given by

$$\frac{1}{g_c J} = \max\left(\sqrt{2(1+\gamma)}, \frac{J_0}{J} + \frac{J}{J_0}\frac{1+\gamma}{2}\right) \tag{S55}$$

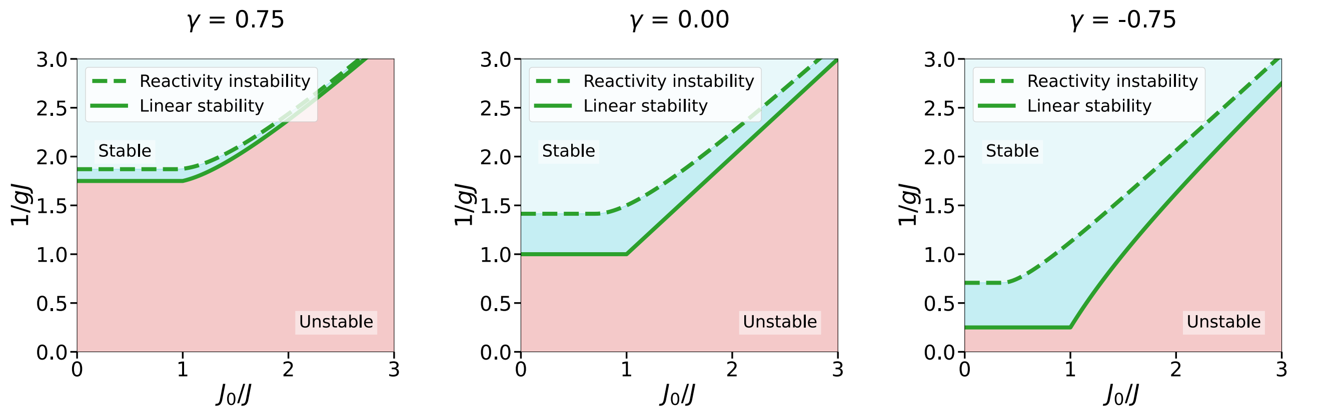

FIG. S15. Phase diagram of the model (noiseless dynamics, $\sigma = 0$) showing the reactivity bifurcation line Eq.(S55) and linear stability line Eq.(42) for different values of reciprocity γ. Between the two lines, a stable but reactive region (green shaded) emerges.

In Fig.S15 we compare the reactivity instability bifurcation lines (dashed, green line), described by Eq.(S55), and the linear stability (solid, green line) given by Eq.(42), for different values of reciprocity γ. The paramagnetic phase, which is the region on which the steady-state $\mathbf{x} = 0$ is linearly stable, contains a (green shaded) region of reactivity, right before entering the phase of linear instability (red shaded). The shape and broadness of such an intermediate region depend, as expected, on the asymmetry parameter γ (see Figure). In particular, in the limit $\gamma \to 1$ in which the synaptic matrix $\mathbf{J}$ becomes symmetric the reactive region needs to disappear, and it shrinks progressively as such a limit is approached.

S.V. NON-FIXED POINT STATIONARY SOLUTIONS, $\sigma = 0$, $\gamma = 0$

In this section we derive results concerning the dynamics of the correlation function in non-fixed point steady-states.

A. Dynamical equation for the correlator

Starting with Eq.(10) and setting $\gamma = 0$ we have

$$\dot{x}(t) = -x(t) + \tanh[J_0 g M(t) + \phi(t)] + \xi(t) \tag{S56}$$

When the system is not at a fixed point, the stochastic term $\phi(t)$ is time-dependent. At stationarity, the joint probability of $\phi(t)$ taking value ϕ at time t and ϕ' at time t' is a bi-variate Gaussian distribution

$$P(\phi, t; \phi', t') = \frac{1}{2\pi\sqrt{\det \boldsymbol{\Delta}(\tau)}} \exp\left(-\frac{1}{2}\boldsymbol{\phi}^T \boldsymbol{\Delta}^{-1}(\tau)\boldsymbol{\phi}\right)$$

with zero average and covariance matrix

$$\boldsymbol{\Delta}(\tau) = \begin{pmatrix} \Delta(0) & \Delta(\tau) \\ \Delta(\tau) & \Delta(0) \end{pmatrix} \tag{S57}$$

where we have denoted with $\boldsymbol{\phi}^T = (\phi, \phi')$, with $\Delta(0) = \langle \phi^2(t) \rangle$ the equal-time correlation (which is independent of t) and with $\Delta(\tau) = \langle \phi(t+\tau)\phi(t) \rangle$ the two-time correlation (which depends only on the time-difference) and we have used $\Delta(\tau) = \Delta(-\tau)$. From Eq.(11) we have $\Delta(\tau) = g^2 J^2 C(\tau)$ for all τ. The marginal $P(\phi, t)$ is then a Gaussian distribution with zero average and variance $\Delta(0) = g^2 J^2 C(0)$. Averaging Eq.(S56) over ϕ and ξ, and setting $\dot{M} = 0$, we get Eq.(22), for any value of σ.

Following[57], an equation for $C(\tau)$ can be obtained by multiplying Eq.(S56) at time t by the same equation at time t',

$$\begin{aligned}(\partial_t + 1)x(t)\,(\partial_{t'} + 1)x(t') = \tanh[J_0 g M + \phi(t)]\,\tanh[J_0 g M + \phi(t')] + \xi(t)\tanh[J_0 g M + \phi(t')] \\ + \xi(t')\tanh[J_0 g M + \phi(t)] + \xi(t)\xi(t')\end{aligned} \tag{S58}$$

averaging over $P(\phi,t;\phi',t')$ and over the Gaussian white noise $\xi(t)$. Using $\partial_{t'}C(t-t') = -\partial_t C(t-t') = -\partial_\tau C(\tau)$ gives Eq.(34) and setting $\sigma = 0$ leads to Eq.(23). For $\sigma = 0$, an equation for $C(0)$ can be obtained by multiplying Eq.(15) times x, using $2x\frac{dx}{dt} = \frac{d}{dt}x^2$ and averaging over ϕ

$$\frac{1}{2}\frac{d}{dt}C(t,t) = -C(t,t) + \langle x(t)\tanh(gJ_0M + \phi(t))\rangle \tag{S59}$$

where we have used $C(t,t) = \langle x^2(t)\rangle$. Substituting

$$\begin{aligned} x(t) &= x_0 e^{-t} + \int_0^t dt'\, e^{-(t-t')}\tanh[J_0 gM + \phi(t')] \\ &= x_0 e^{-t} + \int_0^t d\tau\, e^{-\tau}\tanh[J_0 gM + \phi(t-\tau)] \end{aligned} \tag{S60}$$

in Eq.(S59), taking the large time limit and using $\lim_{t\to\infty} C(t,t) = C(0)$ we finally get

$$C(0) = \int_0^\infty d\tau\, e^{-\tau}\int \frac{d\phi d\phi'}{2\pi\sqrt{g^4J^4\det\mathbf{C}}}\exp\left(-\frac{1}{2g^2J^2}\boldsymbol{\phi}^T\mathbf{C}^{-1}(\tau)\boldsymbol{\phi}\right)\tanh[J_0 gM + \phi]\,\tanh[J_0 gM + \phi'] \tag{S61}$$

which leads to

$$C(0) = \int_0^\infty d\tau\, e^{-\tau}\,\Xi(C(\tau), C(0), M) \tag{S62}$$

At the fixed point $C(\tau) = C(0)\ \forall\ \tau$, this retrieves $C(0) = q$ via $\lim_{C\to C(0)}\Xi(C, C(0), M) = \int \mathcal{D}\psi\tanh^2(J_0 gM + gJ\sqrt{C(0)}\psi)$. However, away from fixed points, determining the stationary value of the persistent order parameter $C(0)$ requires knowledge of the non-persistent (i.e. time-dependent) correlation function $C(\tau)$.

B. Bifurcations of non-fixed point stationary solutions

To study the bifurcations of $C(0)$ from zero, it is convenient to set $C(\tau) = C(0)\kappa(\tau)$, where $-1 \le \kappa(\tau) \le 1$ (as $|C(\tau)| \le C(0)$. Substituting in Eq.(S61), we obtain

$$\begin{aligned} C(0) = \int_0^\infty d\tau\, e^{-\tau}\int \frac{d\phi d\phi'}{2\pi\sqrt{1-\kappa^2(\tau)}}\exp\left(-\frac{1}{2(1-\kappa^2(\tau))}\boldsymbol{\phi}^T\begin{pmatrix} 1 & -\kappa(\tau) \\ -\kappa(\tau) & 1\end{pmatrix}\boldsymbol{\phi}\right) \\ \times\tanh[J_0 gM + gJ\sqrt{C(0)}\phi]\tanh[J_0 gM + gJ\sqrt{C(0)}\phi'] \end{aligned} \tag{S63}$$

From Eq.(22) and Eq.(S63) we see that $(M, C(0)) = (0,0)$ is always a solution. Expanding Eq.(S63) for small M and $C(0)$ we find

$$\begin{aligned} C(0) &= \int_0^\infty d\tau\, e^{-\tau}\int \frac{d\phi d\phi'}{2\pi\sqrt{1-\kappa^2(\tau)}}\exp\left(-\frac{1}{2(1-\kappa^2(\tau))}\boldsymbol{\phi}^T\begin{pmatrix} 1 & -\kappa(\tau) \\ -\kappa(\tau) & 1\end{pmatrix}\boldsymbol{\phi}\right) \\ &\quad\times[J_0 gM + gJ\sqrt{C(0)}\phi][J_0 gM + gJ\sqrt{C(0)}\phi'] \\ &= (gJ_0M)^2 + (gJ^2)C(0)\int_0^\infty d\tau\, e^{-\tau}\kappa(\tau) \end{aligned} \tag{S64}$$

showing that $C(0)$ can bifurcate from zero either at $M = 0$ for $(gJ^2)\int_0^\infty d\tau\, e^{-\tau}\kappa(\tau) = 1$ (spin-glass transition), or when M bifurcates (ferromagnetic transition) i.e. at $gJ_0 = 1$, from equation Eq.(22). As $|C(\tau)| \le C(0)$, bifurcations in $C(\tau)$ cannot precede those of $C(0)$, hence, bifurcations from the paramagnetic state, for non-fixed point steady states, occur at

$$\frac{1}{gJ} = \max\left(\sqrt{\int_0^\infty d\tau\, e^{-\tau}\kappa(\tau)}, \frac{J_0}{J}\right) \tag{S65}$$

For $\kappa(\tau) = 1$, Eq.(S65) retrieves the phase diagram for fixed point solutions, Eq.(4). As $\kappa(\tau) \le 1\,\forall\,\tau$, and $\kappa(\tau) = 1\,\forall\,\tau$ for fixed point solutions, the equation above suggests that fixed point solutions are the first non-trivial solutions to emerge as $1/gJ$ is decreased below one. This is supported by numerical simulations at finite N, shown in Fig.6. Note that only solutions which satisfies $\int_0^\infty d\tau\, e^{-\tau}\kappa(\tau) > 0$ contribute to the spin-glass phase. If $\int_0^\infty d\tau\, e^{-\tau}\kappa(\tau) < 0$, then there is no spin-glass transition and bifurcations occur at $g = 1/J_0$.

C. Shape of the potential $V(C|C(0), M)$

We have shown in Sec. S.V B that, at stationarity, the correlator $C(\tau)$ evolves according to a gradient-descent Eq.(26) on the potential $V(C|C(0), M)$. In order to have a physical motion, the correlator $C(\tau)$ has to be bounded, verifying the condition $|C(\tau)| \leq C(0)$ for $\tau \geq 0$. For the noiseless dynamics (i.e. $\sigma = 0$), where $\dot{C}(0) = 0$, this is equivalent to require that the derivative of the potential satisfies $V'(C(0)|C(0), M) \geq 0$ and $V'(-C(0)|C(0), M) \leq 0$ at the boundaries $C = \pm C(0)$.

One can show that for any M, $V'(C(0)|C(0), M) > 0$ for $0 < C(0) < q$, while $V'(C(0)|C(0), M) < 0$ for any $C(0) > q$, with $V'(q|q, M) = 0$, see Fig.3 (A), (D). Hence, initial conditions $C(0) > q$, are unphysical as they lead to unbounded motion. By diagonalizing $\mathbf{C}$, we can rewrite Eq.(24) as

$$\begin{aligned}\Xi(C, C(0), M) = \int \frac{dxdy}{2\pi} e^{-\frac{x^2}{2}-\frac{y^2}{2}} \tanh\left[J_0 g M + gJx\sqrt{\frac{C(0)+C}{2}} - gJy\sqrt{\frac{C(0)-C}{2}}\right] \\ \times \tanh\left[J_0 g M + gJx\sqrt{\frac{C(0)+C}{2}} + gJy\sqrt{\frac{C(0)-C}{2}}\right]\end{aligned} \tag{S66}$$

which shows that for $M = 0$, $\Xi(C, C(0), 0) = -\Xi(-C, C(0), 0)$, hence $V'(C|C(0), 0) = -V'(-C|C(0), 0)$. This implies $V'(-C(0)|C(0), 0) < 0$ for $0 < C(0) < q$ and $V'(-q|q, 0) = 0$, see Fig.3 (D). Thus, for $M = 0$, any initial condition $0 < C(0) \leq q$ leads to bounded solutions.

On the other hand, for $M \neq 0$, i.e. $J > J_0$, one can show that $V'(C|C(0), M) > 0$ for any $-C(0) \leq C \leq C(0)$ with $0 < C(0) < q$, while $V'(C|q, M) > 0$ for any $-q < C < q$, with $V'(q|q, M) = 0$, see Fig.3 (A). This shows that for any initial condition $0 < C(0) \leq q$, the potential is a monotonic non-decreasing function which has only one stationary point, at the boundary of the physical region $C = C(0) = q$. Hence the only possible bounded steady-state solutions for $M \neq 0$ are the fixed point solutions $C = q$.

In the following, we discuss the shape of the potential for $M = 0$. We start by noting that as $V'(C|C(0), 0) = -V'(-C|C(0), 0)$, $V'(0|C(0), 0) = 0$ for all $C(0)$, hence the potential has a stationary point at $C = 0$, for any initial condition $C(0)$. One can show that this is the *only* stationary point (and in particular a minimum) for $C(0)$ below a threshold value C_{th}. Above this threshold, i.e. for $C_{\text{th}} < C(0) \leq q$, $C = 0$ becomes a maximum and two minima $\pm\bar{C}(C(0))$ develop at either side of $C = 0$, see Fig.3 (D). Numerical analysis shows that $\bar{C}(C(0))$ is a monotonically increasing function of $C(0)$ and that $\bar{C}(q) = q$. The value C_{th} can be determined from the condition $V''(0|C(0), 0) = 0$, which gives

$$\begin{aligned}V''(0|C(0), 0) &= -1 + \frac{1}{J^2 g^2 C_0} \frac{1}{C_0^2} \int \frac{d\phi d\phi'}{2\pi J^2 g^2} e^{-\frac{1}{2J^2g^2}\boldsymbol{\phi}^T \mathbf{C}^{-1} \boldsymbol{\phi}} (\phi \tanh\phi)(\phi' \tanh\phi') \\ &= -1 + \frac{1}{J^2 g^2 C_0^2} \left[\int \frac{d\phi}{\sqrt{2\pi J^2 g^2 C(0)}} e^{-\frac{1}{2J^2g^2C(0)}\phi^2} (\phi \tanh\phi)\right]^2 \\ &= -1 + \frac{1}{C_0} \left[\int \mathcal{D}\psi \psi \tanh(\psi g J \sqrt{C(0)})\right]^2 \\ &= -1 + \frac{1}{C_0} \left[\int \mathcal{D}\psi [1 - \tanh^2(\psi g J \sqrt{C(0)})] g J \sqrt{C(0)}\right]^2 \\ &= -1 + g^2 J^2 \left[1 - \int \mathcal{D}\psi \tanh^2(\psi g J \sqrt{C(0)})\right]^2 = 0\end{aligned} \tag{S67}$$

thus leading to Eq.(31). In Fig.3 (E, F) we have plotted the curve $C_0 = C_{\text{th}}(1/gJ)$ (solid red line), as a function of $1/gJ$, described by Eq.(31). In the paramagnetic region $gJ < 1$, Eq.(31) does not allow real solutions and $C = 0$ is always a minimum. Conversely, in the spin-glass region $gJ > 1$, Eq.(31) always allows a solution $0 \leq C_{\text{th}} \leq q$, as $\int \mathcal{D}\psi \tanh^2(gJ\sqrt{q}\,\psi) \equiv q \geq 1 - 1/gJ$ is always satisfied. In the spin-glass region, for any $0 < C(0) \leq C_{\text{th}}$ the potential is single-well, whereas for any $C_{\text{th}} < C(0) \leq q$ the potential is double-well. Hence different types of motion can arise, depending on the value of $C(0)$, as it is explained in Sec. IV A 2.